CrossMark

J. Fluid Mech. (2015), *vol.* 769, *pp.* 444–481. © Cambridge University Press 2015
doi:10.1017/jfm.2015.121

Air entrainment in dynamic wetting: Knudsen effects and the influence of ambient air pressure

James E. Sprittles†

Mathematics Institute, University of Warwick, Coventry CV4 7AL, UK

(Received 17 October 2014; revised 11 January 2015; accepted 18 February 2015;
first published online 25 March 2015)

Recent experiments on coating flows and liquid drop impact both demonstrate that wetting failures caused by air entrainment can be suppressed by reducing the ambient gas pressure. Here, it is shown that non-equilibrium effects in the gas can account for this behaviour, with ambient pressure reductions increasing the mean free path of the gas and hence the Knudsen number Kn. These effects first manifest themselves through Maxwell slip at the boundaries of the gas, so that for sufficiently small Kn they can be incorporated into a continuum model for dynamic wetting flows. The resulting mathematical model contains flow structures on the nano-, micro- and millimetre scales and is implemented into a computational platform developed specifically for such multiscale phenomena. The coating flow geometry is used to show that for a fixed gas–liquid–solid system (*a*) the increased Maxwell slip at reduced pressures can substantially delay air entrainment, i.e. increase the 'maximum speed of wetting', (*b*) unbounded maximum speeds are obtained, as the pressure is reduced only when slip at the gas–liquid interface is allowed for, and (*c*) the observed behaviour can be rationalised by studying the dynamics of the gas film in front of the moving contact line. A direct comparison with experimental results obtained from a dip-coating process shows that the model recovers most trends but does not accurately predict some of the high viscosity data at reduced pressures. This discrepancy occurs because the gas flow enters the 'transition regime', so that more complex descriptions of its non-equilibrium nature are required. Finally, by collapsing onto a master curve experimental data obtained for drop impact in a reduced pressure gas, it is shown that the same physical mechanisms are also likely to govern splash suppression phenomena.

Key words: coating, contact lines, rarefied gas flow

1. Introduction

The behaviour of liquid–solid–gas contact lines, at which an ambient gas is displaced by a liquid spreading over a solid, is the key element of many technological processes, ranging from coating flows used to apply thin liquid films to substrates (Weinstein & Ruschak 2004) to 3D printers being developed to economically produce bespoke geometrically complex structures (Derby 2010). Often, limitations on the operating devices are imposed by 'wetting failure', which occurs when the liquid can

† Email address for correspondence: J.E.Sprittles@warwick.ac.uk

https://doi.org/10.1017/jfm.2015.121 Published online by Cambridge University Press

no longer completely displace the gas at the contact line. In coating technologies, this leads to the entrainment of gas bubbles into the liquid film, which destroy its carefully tuned material properties, while in drop-based flows entrainment of air under the moving contact line promotes the formation of splashes, which, again, are usually undesirable. Consequently, an understanding of the physical mechanisms that control wetting failure and, where possible, delay of this occurrence by manipulating the material parameters, flow geometry, etc. to ever increasing wetting speeds are some of the key aims of research into dynamic wetting.

Recent experimental studies have discovered new ways in which to delay the onset of wetting failures. Specifically, in both coating flows (Benkreira & Khan 2008; Benkreira & Ikin 2010) and drop impact phenomena (Xu, Zhang & Nagel 2005; Xu 2007) it has been shown that a sufficient reduction in the pressure of the ambient gas, by approximately a factor of ten in the former case and even less in the latter, can suppress wetting failures. This result was unexpected, as until the work of Xu *et al.* (2005) it was assumed that the gas dynamics can either be entirely neglected or, as found in coating research, only influences the system behaviour through viscous forces that act in the thin gas film in front of the moving contact line (Kistler 1993). However, the significance of the viscous forces in the gas is usually characterised by the viscosity ratio between the gas and the liquid, and this remains unchanged by variations in gas pressure. Why then, would reductions in ambient pressure have any influence on the contact line dynamics?

An interpretation of the aforementioned phenomena, suggested in a number of different contexts, is that the reduction in ambient gas pressure, which leads to a corresponding decrease in gas density, increases the mean free path in this phase so that non-equilibrium gas dynamics (Chapman & Cowling 1970), also referred to as rarefied gas dynamics (Cercignani 2000), become important (Benkreira & Ikin 2010; Duchemin & Josserand 2012; Marchand *et al.* 2012). Specifically, boundary slip is generated in the gas, whose magnitude is proportional to the mean free path and thus whose influence is increased by reductions in gas pressure. The increased slip allows gas trapped in thin films between the solid and the free surface to escape more easily, so that the lubrication forces generated by the gas are reduced and its influence is negated.

For drop impact phenomena, the literature of which has been previously reviewed (Rein 1993; Yarin 2006), alterations in the lubrication forces could be important either (*a*) in the thin air cushion that exists under the drop before it impacts the solid (Thoroddsen, Etoh & Takehara 2005; Bouwhuis *et al.* 2012) and/or (*b*) in the gas film formed in front of the advancing contact line after the drop has impacted the solid (Riboux & Gordillo 2014), see figure 1. Theoretical work has also focused on either (*a*) the pre-impact stage (Smith, Li & Wu 2003; Mani, Mandre & Brenner 2010; Mandre & Brenner 2012) or (*b*) the post-impact spreading phase where, with a few exceptions (Schroll *et al.* 2010), the gas is usually considered to be passive (Bussmann, Chandra & Mostaghimi 2000; Eggers *et al.* 2010; Sprittles & Shikhmurzaev 2012*a*). It is a complex problem to distinguish how each of these processes influences the spreading dynamics of the drop, from both a theoretical and an experimental perspective, due to the inherently multiscale nature of the phenomenon. As a result, it remains an area of intensive debate to establish how reductions in ambient pressure suppress splashing (Driscoll & Nagel 2011; Kolinski *et al.* 2012; de Ruiter *et al.* 2012), with recent experimental results on the impact stage being particularly interesting (Kolinski, Mahadevan & Rubinstein 2014; de Ruiter *et al.* 2015; Liu, Tan & Xu 2015).

https://doi.org/10.1017/jfm.2015.121 Published online by Cambridge University Press

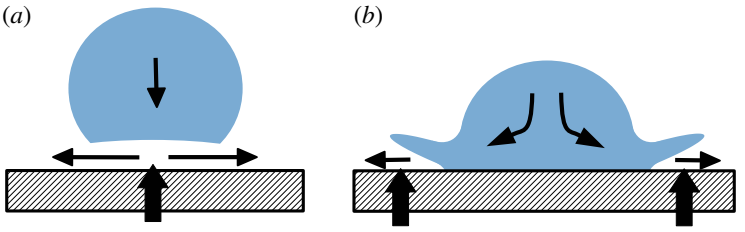

FIGURE 1. (Colour online) Sketch illustrating the influence of gas flow on the drop impact phenomenon. The behaviour of the gas, in the regions indicated by black arrows, affects both (*a*) the pre-impact and (*b*) the post-impact spreading dynamics of the drop.

In contrast to drop-based dynamics, for the dip-coating flow investigated in Benkreira & Khan (2008) mechanism (*a*) does not exist, as up until the point of wetting failure, the liquid remains in contact with the solid and the motion is steady. Therefore, study of this process allows us to isolate the influence of changes in ambient pressure on the behaviour of a moving contact line, i.e. effect (*b*), without any of the aforementioned complications that are inherent to the drop impact phenomenon. This is the path that will be pursued in the present work, with drop dynamics only reconsidered again in § 7 where, having characterised fully (*b*), our results enable us to infer some conclusions about drop splashing phenomena.

1.1. *Experimental observations in dip coating*

The experimental set-up constructed in Benkreira & Khan (2008) is for dip coating, where a plate/tape is continuously run through a liquid bath (figure 2) and gradually increased in speed until air is entrained into the liquid. The speed at which this first occurs is called the 'maximum speed of wetting' and will be denoted by $U_c^\star$, where stars will be used throughout to denote dimensional quantities. In contrast to previous works (Burley & Kennedy 1976; Blake & Shikhmurzaev 2002), the ambient gas pressure $P_g^\star$ can be reduced from its atmospheric value by up to a factor of a hundred by mounting this apparatus inside a vacuum chamber. Silicone oils of differing viscosities are used as the coating liquid, because their relatively low volatility (compared with, say, water–glycerol mixtures) ensures no significant evaporation when the ambient pressure is reduced. This work is extended in Benkreira & Ikin (2010) to consider also a range of different ambient gases (air, carbon dioxide and helium). The key results from Benkreira & Khan (2008) can be summarised as follows.

(*a*) For a given liquid–solid–gas system, $U_c^\star$ can be increased by reducing $P_g^\star$.

(*b*) There is very little variation in $U_c^\star$ until $P_g^\star$ is approximately a tenth of its atmospheric value. Further reductions in $P_g^\star$ lead to sharp increases in $U_c^\star$.

(*c*) For sufficiently low $P_g^\star$, it is possible for high-viscosity liquids to have a larger value of $U_c^\star$ than lower-viscosity ones (the opposite of what occurs at atmospheric pressure).

In addition to these findings, in Benkreira & Ikin (2010) the following is shown.

(*d*) For a given value of $P_g^\star$, use of a gas with a larger mean free path increases $U_c^\star$.

https://doi.org/10.1017/jfm.2015.121 Published online by Cambridge University Press

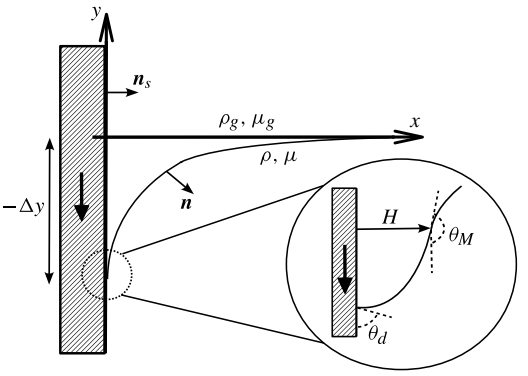

FIGURE 2. Sketch of the dip-coating flow configuration, showing a free surface formed between a liquid (below) and gas (above), with density and viscosity ρ, μ and ρ_g, μ_g, respectively. The free surface meets a solid surface at a contact line, which is a distance Δy below the height of the surface ($y=0$). The unit vectors normal to the free-surface and solid are, respectively, $\boldsymbol{n}$ and $\boldsymbol{n}_s$. The inset shows that the free surface meets the solid at a contact angle θ_d but that a finite distance away has an apparent angle θ_M at an inflection point in the surface profile where the film has height H.

In Benkreira & Ikin (2010), the aforementioned experimental observations are assumed to be caused by non-equilibrium effects in the gas which become significant at sufficiently low pressures. These effects, most notably slip at the boundaries of the gas film, are interpreted in terms of an 'effective gas viscosity' whose magnitude is reduced with decreases in ambient gas pressure. Use of appropriate values for this parameter, obtained from measurements of the resistance of a gas trapped between parallel oscillating plates (Andrews & Harris 1995), allows the data to be collapsed onto a single curve (figure 9*b* in Benkreira & Ikin 2010) and highlights the influence of non-equilibrium effects.

Although the effective viscosity may be a useful concept when trying to qualitatively interpret the experimental findings, as an integral property of the system it will not enable us to formulate a local fluid mechanical model for this problem. In particular, the dependence of the effective gas viscosity on the ambient gas pressure which is used in Benkreira & Ikin (2010) was obtained in Andrews & Harris (1995) for a gas film of constant height 2 μm and will be different for other film profiles. In reality, the gas film height will vary all the way from the contact line to the far field, where a film can no longer be defined so that the notion of an effective viscosity no longer makes sense. Instead, we must look to capture the local physical mechanisms that alter the gas film dynamics at reduced pressures.

1.2. *Mathematical modelling of dynamic wetting phenomena*

We consider the various levels of description that can be used to describe dynamic wetting phenomena depending on how the gas dynamics are accounted for, with the simplest case first.

1.2.1. *Dynamic wetting in a passive gas*

In many cases, the viscosity and density ratios indicate that the gas can be treated as dynamically passive. Then, mathematical models for the liquid dynamics must address

https://doi.org/10.1017/jfm.2015.121 Published online by Cambridge University Press

two key aspects. First, the classical fluid mechanical model, with no-slip at fluid–solid boundaries, has no solution (Huh & Scriven 1971; Shikhmurzaev 2006). This is the so-called 'moving contact-line problem'. Second, the contact angle, which is seen to vary at experimental resolutions (Hoffman 1975; Blake & Shikhmurzaev 2002), must be prescribed as a boundary condition on the free-surface shape. A review of the various classes of models proposed to address these issues can be found in chap. 3 of Shikhmurzaev (2007).

To overcome the moving contact-line problem, initially identified in Huh & Scriven (1971), it is often assumed that some degree of slip occurs at the fluid–solid boundary (Dussan V 1976). Methods for predicting the 'slip length' of an arbitrary liquid–solid interface are not well developed, but estimates suggest that it is in the range 1–10 nm for simple liquids (Lauga, Brenner & Stone 2007).

The treatment of the dynamic contact angle remains a highly contentious issue. The main question is whether or not the experimentally observed variation in the 'apparent angle' (Wilson *et al.* 2006) is caused entirely by the bending of the free surface below the resolution of the experiment, i.e. by the 'viscous bending' mechanism quantified in Cox (1986) and measured in Dussan V, Ramé & Garoff (1991) and Ramé & Garoff (1996), or whether the actual contact angle (sometimes referred to as the 'microscopic angle') also varies. In either case, the apparent angle depends on the capillary number, which is the dimensionless contact-line speed, but in the former case the actual angle remains fixed while in the latter this angle varies, as in the molecular kinetic theory (Blake & Haynes 1969). In more complex models, the angle can also depend on the flow field itself, as in the interface formation model (Shikhmurzaev 2007).

Models in which the contact angle is considered to be constant have been popular in recent years for investigating air entrainment phenomena and have produced a number of promising results (Marchand *et al.* 2012; Vandre, Carvalho & Kumar 2012, 2013, 2014; Chan *et al.* 2013). What is clear from simulations is that viscous bending of the free surface becomes significant as the point of air entrainment is approached, and cannot be neglected. What remains unclear is whether this mechanism is sufficient to account for the experimentally observed dynamics of the apparent contact angle, particularly given that precise measurements of the magnitude of slip on the liquid–solid interface are lacking. These difficulties have stimulated fundamental research into the contact-line region dynamics using molecular dynamics techniques (De Coninck & Blake 2008), but, as can be seen from a recent collection of papers (Velarde 2011) and review articles (Blake 2006; Snoeijer & Andreotti 2013), intense debate remains about the topic.

The focus of this work is to characterise the effects that the gas dynamics can have on dynamic wetting phenomena, and, consequently, the simplest possible model for the other aspects will be used. Specifically, slip at the liquid–solid interface will be captured using the Navier condition (Navier 1823), as commonly used in dynamic wetting models (Hocking 1976; Huh & Mason 1977), and the contact angle will be taken as a parameter that is fixed at its equilibrium value. The result is a 'conventional model', and a comprehensive review of all such models that can be 'built' is given in chap. 9 of Shikhmurzaev (1997). More complex models can easily be constructed on top of the model used here, but in the present context would distract from the main focus of this work.

1.2.2. *In a viscous gas*

It is now well recognised that at sufficiently high coating speeds a thin film of gas forms in front of the moving contact line, as observed experimentally by laser-Doppler

https://doi.org/10.1017/jfm.2015.121 Published online by Cambridge University Press

velocimetry in Mues, Hens & Boiy (1989). The thin nature of the film means that despite the large viscosity ratio, lubrication forces enhance the influence of the gas dynamics so that they cannot be neglected. As coating speeds are increased, the resistance this film creates to contact-line motion eventually becomes sufficiently large that it is entrained into the liquid (Marchand *et al.* 2012; Vandre *et al.* 2013). Therefore, to study the phenomenon of air entrainment and wetting failures, any theory developed must account for the dynamics of the viscous gas as well as the liquid.

In formulating a model for the gas dynamics one again encounters the moving contact-line problem, namely that if no-slip is used then the contact line cannot move. Consequently, slip has also often been applied on the solid–gas boundary with a magnitude, measured by the slip length, either explicitly stated to be the same as in the liquid (Vandre *et al.* 2013) or implicitly assumed to be so (Cox 1986). In other words, slip is usually used as a mathematical fix to circumvent the moving contact-line problem, rather than as a physical effect whose magnitude can significantly alter the flow.

1.2.3. *In a non-equilibrium gas*

Experimental observations in Marchand *et al.* (2012), where the gas film entrained by a plunging plate was measured using optical methods, suggest that for relatively viscous liquids the characteristic film thickness is rather small, in the range $H^\star \sim 1$–15 μm. For flows where there is an external load on the film, such as in curtain coating, the film thickness is likely to be even smaller. Consequently, the film dimensions become comparable with the mean free path in the gas $\ell^\star$, so that the Knudsen number $Kn_H = \ell^\star/H^\star$, characterising the importance of non-equilibrium gas effects, becomes non-negligible, particularly at reduced pressures. For example, a factor of 10 decrease in the ambient pressure of air, achieved in both Xu *et al.* (2005) and Benkreira & Khan (2008), gives a value of $\ell^\star = 0.7$ μm, so that $Kn_H \sim 0.1$. In this case, one may expect that non-equilibrium effects in the gas film will have a significant impact on its dynamics, and we must consider how this can be incorporated into our dynamic wetting model.

Non-equilibrium effects first manifest themselves at the boundaries of the gas and can be accounted for by relaxing the no-slip condition to allow for boundary slip while continuing to use the Navier–Stokes equations in the bulk. This approach remains accurate for $Kn_H < 0.1$, during which gas flow is said to be in the 'slip regime', after which Knudsen layers will begin to occupy the entire gas film, so that the scale separation between boundary and bulk effects no longer exists.

In Maxwell (1879), a slip condition was derived for the 'micro-slip' at the actual boundary of the gas, whose mathematical form remains the same, when $Kn_H \ll 1$, if 'macro-slip' across a Knudsen layer of size $\sim\ell^\star$ is also accounted for, see § 3.5 of Cercignani (2000). We shall henceforth refer to the discontinuity in tangential velocity as 'Maxwell slip', which at an impermeable boundary is generated by the shear stress acting on that interface from the gas phase. For two-dimensional isothermal flow, the component of velocity $u_g^\star$, where subscript g will denote properties of the gas, adjacent to a stationary planar surface located at $y = 0$ is, in dimensional terms, given by

$$a\,\ell^\star \frac{\partial u_g^\star}{\partial y^\star} = u_g^\star, \tag{1.1}$$

where the coefficient of proportionality a can depend on both the properties of the micro-slip, which will depend on the fraction of molecules that reflect diffusively and

https://doi.org/10.1017/jfm.2015.121 Published online by Cambridge University Press

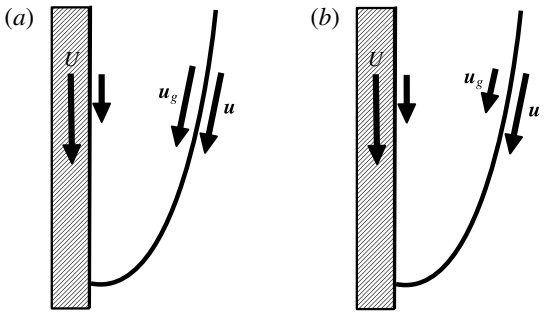

FIGURE 3. The effect of Maxwell slip on the gas flow. When (*a*) $A = 0$ slip is present at the gas–solid boundary but turned off at the gas–liquid boundary, so that $\boldsymbol{u}_g = \boldsymbol{u}$, while (*b*) for $A = 1$ it is present on both interfaces.

those that are purely specular, and the macro-slip generated across a Knudsen layer. In practice, unless surfaces are molecularly smooth we will have $a \sim 1$ (Millikan 1923; Allen & Raabe 1982; Agarwal & Prabhu 2008) and, for simplicity, we will henceforth take $a = 1$.

The Maxwell-slip condition (1.1) has the same form as the slip conditions that have often been used in dynamic wetting flows to circumvent the moving contact-line problem in the gas, but occurs naturally here from the consideration of non-equilibrium effects. Notably, this means that accurate values of the slip length can easily be obtained by knowing the mean free path in the gas, in contrast to the slip length in the liquid which is notoriously difficult to determine. Furthermore, the approach taken here suggests that slip will also be present at the gas–liquid boundary (i.e. the free surface), as demonstrated by experiments dating back to Millikan (1923). This effect is shown in figure 3, where the parameter A is used to change between the usual condition of continuity of velocity across the gas–liquid interface ($A = 0$) and Maxwell slip ($A = 1$).

Slip at the gas–liquid boundary has been accounted for in some models for the gas film in drop impact (Mani *et al.* 2010; Duchemin & Josserand 2012), and in great detail for drop collisions (Sundararajakumar & Koch 1996), but is yet to be routinely incorporated into dynamic wetting models. In most cases where slip on the gas–solid interface is accounted for, the same effect on the gas–liquid surface is not considered (Vandre *et al.* 2013; Riboux & Gordillo 2014). The only progress in this direction has been achieved in Marchand *et al.* (2012), where non-equilibrium effects are accounted for by modifying the viscosity in the gas. However, this is achieved by using an empirical expression for the effective viscosity which suffers from the same issues as mentioned previously, namely a reliance on the lubrication approximation that does not enable one to fully formulate a uniformly valid local fluid mechanical problem.

In order to apply Maxwell slip at curved moving surfaces, the tensorial expression is required (Lockerby *et al.* 2004). Specifically, for gas flow adjacent to a surface that moves with velocity $\boldsymbol{u}^\star$ and has normal $\boldsymbol{n}$ pointing into the gas, we have

$$\ell^\star \boldsymbol{n} \cdot (\nabla \boldsymbol{u}_g^\star + [\nabla \boldsymbol{u}_g^\star]^{\mathrm{T}}) \cdot (\boldsymbol{I} - \boldsymbol{nn}) = \boldsymbol{u}_{g\parallel}^\star - \boldsymbol{u}_\parallel^\star, \tag{1.2}$$

where the subscript $\parallel$ denotes the components of a vector tangential to the surface, which can be obtained for an arbitrary vector $\boldsymbol{a}$ using $\boldsymbol{a}_\parallel = \boldsymbol{a} \cdot (\boldsymbol{I} - \boldsymbol{nn})$, where $\boldsymbol{I}$ is the metric tensor of the coordinate system.

https://doi.org/10.1017/jfm.2015.121 Published online by Cambridge University Press

If the gas is modelled as being composed of 'hard spheres', then the mean free path is related to the temperature $T^\star$ and ambient pressure $P_g^\star$ by $\ell^\star = k_B^\star T^\star/(\sqrt{2}\pi P_g^\star (l_{mol}^\star)^2)$, where $l_{mol}^\star$ is the molecular diameter and $k_B^\star$ is Boltzmann's constant. Notably, if local variations in gas pressure about $P_g^\star$ are small, as confirmed in § 4.5, then for a given ambient pressure $\ell^\star$ is approximately constant throughout the entire gas phase. In practice, when considering the dependence of the mean free path of a gas on the ambient pressure at a fixed temperature it is convenient to use the expression

$$\bar{\ell} \equiv \frac{\ell^\star}{\ell_{atm}^\star} = \frac{P_{g,atm}^\star}{P_g^\star} \equiv 1/\bar{P}_g, \tag{1.3}$$

where $\bar{P}_g$ is the gas pressure normalised by its atmospheric value. At atmospheric pressure, air has a mean free path $\ell_{atm}^\star = 0.07$ μm and other commonly encountered gases take similar values $\ell_{atm}^\star \sim 0.1$ μm.

Although the Knudsen number in the gas film Kn_H is of most interest, this can only be obtained once our computations have allowed us to find $H^\star$. Before then, the Knudsen number based on our characteristic scale $Kn = \ell^\star/L^\star$, where $L^\star \sim 1$ mm is the capillary length, must be used. Noting that the dimensionless mean free path at atmospheric pressure is $\ell_{atm} = \ell_{atm}^\star/L^\star$, the resulting expression for Kn takes the form

$$Kn = \frac{\ell_{atm}}{\bar{P}_g}, \tag{1.4}$$

so that the explicit dependence on pressure reduction becomes clear.

1.3. *Overview*

This work will answer the following questions.

(*a*) Can increases in Maxwell slip, caused by experimentally attainable reductions in ambient gas pressure, significantly raise the maximum speed of wetting?

(*b*) Does slip on the liquid–gas interface, usually neglected in this class of flows, have a substantial effect on the dynamic wetting process?

(*c*) Will the magnitude of the Knudsen number based on the gas film height Kn_H be small enough for the gas flow to remain in the 'slip regime'?

(*d*) Is it possible to collapse the data from Xu *et al.* (2005) onto a master curve by assuming that non-equilibrium gas effects are responsible for splash suppression in drop impact?

The paper is organised as follows. In § 2 the dip-coating problem will be formulated and dimensionless parameters will be identified. The mathematical model for this process will be seen to be inherently multiscale, with flow dynamics on the nano-, micro- and milli-metre scale caused by, respectively, slip in the liquid, slip in the gas and capillarity. The computation of such multiscale flows is challenging, and neglecting to resolve all scales in the problem yields inaccurate results (Sprittles & Shikhmurzaev 2012*c*). In § 3, the application of a computational framework developed in Sprittles & Shikhmurzaev (2012*c*, 2013) to this problem is described, which resolves all scales, and our method for defining a maximum speed of wetting is shown. Benchmark computations performed at atmospheric pressure are provided in appendix A. In § 4 the effects of the non-equilibrium gas dynamics on a base state are analysed and the gas flow is described in a lubrication setting. Subsequently, in § 5, a parametric study of the new system is conducted which allows us to identify the importance of the various competing physical mechanisms in the experimentally verifiable regimes before, in § 6, directly comparing our computations

https://doi.org/10.1017/jfm.2015.121 Published online by Cambridge University Press

with experimental data. The implications of these findings for the drop impact phenomenon are considered in § 7. Finally, in § 8, potential avenues of enquiry for future theoretical and experimental development in this area are highlighted.

2. Problem formulation

We consider the flow generated by the steady motion of a smooth chemically homogeneous solid surface which is driven through a liquid–gas free surface in a direction aligned with gravity at a constant speed $U^\star$ (see figure 2). A characteristic length scale for this problem is given by the capillary length $L^\star = \sqrt{\sigma^\star/((\rho^\star - \rho_g^\star)g^\star)} \simeq \sqrt{\sigma^\star/(\rho^\star g^\star)}$, where $\sigma^\star$ is the surface tension of the liquid–gas surface, which is assumed to be constant, $g^\star$ is the acceleration due to gravity and $\rho^\star$, $\rho_g^\star$ are the densities in the liquid and gas respectively, with $\rho_g^\star/\rho^\star \ll 1$ in the liquid–gas systems of interest, so that the capillary length can be determined solely from the liquid density. The scale for pressure is $\mu^\star U^\star/L^\star$, where $\mu^\star$ is the viscosity of the liquid and $\mu_g^\star$ will be its value in the gas.

2.1. *Bulk equations*

For compressibility effects in the liquid and the gas to be negligible we require that the Mach number $Ma = U^\star/c^\star$ in each phase remains small, where $c^\star$ is the speed of sound. Given that $U^\star < 1$ m s^{-1} and $c^\star > 100$ m s^{-1} in all cases considered, we have $Ma < 0.01$. However, this is not a sufficient condition for the flow to be considered incompressible, especially when there are thin films of gas present along which pressure can vary significantly, see § 4.5 of Gad-el-Hak (2006). Here, we will assume that the flow in both phases can be described by the steady incompressible Navier–Stokes equations, and in § 4.5 the validity of this assumption will be confirmed from *a posteriori* calculations. Therefore, we have

$$\nabla \cdot \boldsymbol{u} = 0, \quad Ca\,\boldsymbol{u} \cdot \nabla \boldsymbol{u} = Oh^2 \left(\nabla \cdot \boldsymbol{P} + \hat{\boldsymbol{g}}/Ca\right), \tag{2.1}$$

$$\nabla \cdot \boldsymbol{u}_g = 0, \quad \bar{\rho}\, Ca\,\boldsymbol{u}_g \cdot \nabla \boldsymbol{u}_g = Oh^2 \left(\nabla \cdot \boldsymbol{P}_g + \bar{\rho}\,\hat{\boldsymbol{g}}/Ca\right), \tag{2.2}$$

where the stress tensors in the liquid and gas are, respectively,

$$\boldsymbol{P} = -p\boldsymbol{I} + [\nabla \boldsymbol{u} + (\nabla \boldsymbol{u})^{\mathrm{T}}] \quad \text{and} \quad \boldsymbol{P}_g = -p_g \boldsymbol{I} + \bar{\mu}[\nabla \boldsymbol{u}_g + (\nabla \boldsymbol{u}_g)^{\mathrm{T}}]. \tag{2.3a,b}$$

Here, $\boldsymbol{u}$ and $\boldsymbol{u}_g$ are the velocities in the liquid and gas; p and p_g are the local pressures in the liquid and gas, in contrast to the uppercase P that is used for the ambient pressure in the gas; $Ca = \mu^\star U^\star/\sigma^\star$ is the capillary number based on the viscosity of the liquid; the viscosity ratio is $\bar{\mu} = \mu_g^\star/\mu^\star$; the ratio of gas to liquid densities is $\bar{\rho} = \rho_g^\star/\rho^\star$; and $\hat{\boldsymbol{g}}$ is a unit vector aligned with the gravitational field. The Ohnesorge number $Oh = \mu^\star/\sqrt{\rho^\star \sigma^\star L^\star}$ has been chosen as a dimensionless parameter, instead of the Reynolds number $Re = Ca/Oh^2 = \rho^\star U^\star L^\star/\mu^\star$, as for a given liquid–solid–gas combination Oh will remain constant, i.e. it will depend solely on material parameters and be independent of contact-line speed.

2.2. *Boundary conditions at the gas–solid surface*

Conditions of impermeability and Maxwell slip give

$$\boldsymbol{u}_g \cdot \boldsymbol{n}_s = 0, \quad Kn\,\boldsymbol{n}_s \cdot \boldsymbol{P}_g \cdot (\boldsymbol{I} - \boldsymbol{n}_s\boldsymbol{n}_s) = \boldsymbol{u}_{g\parallel} - \boldsymbol{U}_\parallel, \tag{2.4a,b}$$

where $\boldsymbol{U}$ is the velocity of the solid and the normal to the solid surface is denoted as $\boldsymbol{n}_s$.

https://doi.org/10.1017/jfm.2015.121 Published online by Cambridge University Press

2.3. *Boundary conditions at the liquid–gas free surface*

On the free surface, whose location must be obtained as part of the solution, for a steady flow the kinematic equation and continuity of the normal component of velocity give that

$$\boldsymbol{u}\cdot\boldsymbol{n}=\boldsymbol{u}_g\cdot\boldsymbol{n}=0, \tag{2.5}$$

where $\boldsymbol{n}$ is the normal to the surface pointing into the liquid phase. These equations are combined with the standard balance of stresses with capillarity that give

$$\boldsymbol{n}\cdot(\boldsymbol{P}-\boldsymbol{P}_g)\cdot(\boldsymbol{I}-\boldsymbol{nn})=\boldsymbol{0},\quad \boldsymbol{n}\cdot(\boldsymbol{P}-\boldsymbol{P}_g)\cdot\boldsymbol{n}=\nabla\cdot\boldsymbol{n}/Ca. \tag{2.6a,b}$$

Equations (2.5) and (2.6) are usually combined with a condition stating that the velocity tangential to the interface is continuous across it, $\boldsymbol{u}_{g\parallel}=\boldsymbol{u}_{\parallel}$. However, when Maxwell slip is accounted for this is replaced with

$$-A\,Kn\,\boldsymbol{n}\cdot\boldsymbol{P}_g\cdot(\boldsymbol{I}-\boldsymbol{nn})=\boldsymbol{u}_{g\parallel}-\boldsymbol{u}_{\parallel}, \tag{2.7}$$

where the minus sign occurs because the normal points into the liquid. By setting $A=0$, Maxwell slip can be 'turned off' at the gas–liquid interface, see figure 3, as has been the case in previous dynamic wetting works which only consider slip at the solid boundary.

2.4. *Boundary conditions at the liquid–solid surface*

The standard conditions of impermeability and Navier slip give

$$\boldsymbol{u}\cdot\boldsymbol{n}_s=0,\quad l_s\,\boldsymbol{n}_s\cdot\boldsymbol{P}\cdot(\boldsymbol{I}-\boldsymbol{n}_s\boldsymbol{n}_s)=\boldsymbol{u}_{\parallel}-\boldsymbol{U}_{\parallel}, \tag{2.8a,b}$$

where $l_s=l_s^\star/L^\star$ is the dimensionless slip length based on the (dimensional) slip length at the liquid–solid interface $l_s^\star$. This parameter has no relation to the slip coefficient in the gas which was based on the mean free path $\ell^\star$. In other words, although Maxwell slip and Navier slip have the same mathematical form, their physical origins differ and thus there is no reason to expect their coefficients to have similar magnitudes.

2.5. *Liquid–solid–gas contact line*

Equation (2.6*b*) requires a boundary condition at the contact line which is given by prescribing the contact angle θ_d satisfying

$$\boldsymbol{n}\cdot\boldsymbol{n}_s=-\cos\theta_d. \tag{2.9}$$

Here, our focus is on understanding the effects of the gas dynamics on the dynamic wetting flow, so that we will take the simplest option of assuming θ_d to be a constant. More complex implementations, such as those in Sprittles & Shikhmurzaev (2013), can be considered in future research.

2.6. *'Far-field' conditions*

Dip coating is usually conducted in a tank of finite size whose dimensions are large enough not to alter the dynamics close to the contact line, as confirmed in Benkreira

https://doi.org/10.1017/jfm.2015.121 Published online by Cambridge University Press

& Khan (2008). The influence of system geometry, or 'confinement', on the dynamic wetting process is well known (Ngan & Dussan V 1982), and, in particular, has been used to delay air entrainment (Vandre *et al.* 2012), but this effect is not the focus of the present work. Therefore, the 'far-field' boundaries of our domain, which are assumed to be no-slip solids, $\boldsymbol{u} = \boldsymbol{u}_g = \boldsymbol{0}$, are set sufficiently far from the contact line that they have no influence on the dynamic wetting process. Where the free surface meets the far field it is assumed to be perpendicular to the gravitational field, i.e. 'flat', so that $\boldsymbol{n} \cdot \hat{\boldsymbol{g}} = 1$. In practice, setting the far field (dimensionally) to be twenty capillary lengths from the contact line was found to be sufficiently remote.

3. Computational framework

Dynamic wetting and dewetting flows have often been investigated using the simplifications afforded by the lubrication approximation (Voinov 1976; Eggers 2004). However, for the two-phase flow considered here, this approximation cannot simultaneously be valid in each phase, i.e. the liquid and gas phases cannot both be thin films. As shown in recent papers (Marchand *et al.* 2012; Vandre *et al.* 2013), plausible extensions in the spirit of the lubrication approach can be attempted, but their accuracy can only be ascertained from comparisons with full computations and is unlikely to be acceptable at larger capillary numbers where the contact-line region cannot be considered as 'localised'.

At present, to obtain accurate solutions to the mathematical model formulated in § 2, one is left with no option other than to use computational methods.

Computationally, resolution of all scales in the problem is particularly important to ensure that our contact line (2.9) is applied to the 'actual' or 'microscopic' angle θ_d, rather than the 'apparent one' $\theta_{app} = \theta_{app}(s)$, i.e. the angle of the free surface at a finite distance s from the contact line. Although the apparent angle can, in certain circumstances, be related to the actual angle (Cox 1986), this will not be true at the high capillary numbers observed in coating flows, particularly when non-standard gas dynamics are included.

Here, the gas dynamics will be built into a finite element framework developed in Sprittles & Shikhmurzaev (2012*c*, 2013) to capture dynamic wetting problems and then extended to consider two-phase flow problems in our work on the coalescence of liquid drops (Sprittles & Shikhmurzaev 2014*b*). Notably, this code captures all physically relevant length scales in the problem, from the slip length $l_s^\star \sim 10$ nm up to the capillary length $L^\star \sim 1$ mm, meaning that at least six orders of magnitude in spatial scale are resolved. As a step-by-step user-friendly guide to the implementation has been provided in Sprittles & Shikhmurzaev (2012*c*), only the main details will be recapitulated here alongside some aspects that are specific to the present work.

The code uses the arbitrary Lagrangian Eulerian scheme, based on the method of spines (Ruschak 1980; Kistler & Scriven 1983), to capture the evolution of the free surface in two-dimensional or three-dimensional axisymmetric flows. Both coating flows, which are often time-independent, as well as unsteady flows such as drop impact (Sprittles & Shikhmurzaev 2012*b*), drop coalescence (Sprittles & Shikhmurzaev 2012*a*, 2014*a*,*b*) and bubble formation (Simmons, Sprittles & Shikhmurzaev 2015) have been considered. It has been confirmed that the code accurately captures viscous, inertial and capillarity effects, even when the mesh undergoes large deformations which inevitably occur when $Ca \sim 1$.

The mesh is graded so that small elements can be used near the moving contact line to resolve the slip length while larger elements are used where only scales associated

https://doi.org/10.1017/jfm.2015.121 Published online by Cambridge University Press

with the bulk flow are present. Consequently, the computational cost is relatively low, so that even for the highest resolution meshes used in this work, for a given liquid–solid–gas combination the entire map of, say, Ca versus contact line elevation (Δy) can be mapped in just a few hours on a standard laptop.

Computations at high Ca, roughly those for which $Ca > 0.1$, are notoriously difficult as (*a*) the free surface becomes increasingly sensitive to the global flow and (*b*) regions of high curvature at the contact line require spatial resolution on scales at or below the slip length l_s. Both factors hinder the ease with which converged solutions can be obtained, and these issues are compounded when Oh is small, indicating the importance of nonlinear inertial effects. For all parameter sets computed, converged solutions can always be obtained for $Ca \leqslant 2$, which compares very favourably with previous works, so that this is chosen as an upper cutoff for the results of our parametric study.

3.1. *Benchmark calculations for the maximum speed of wetting*

In coating flows, one would like to know for a given liquid–solid–gas combination the wetting speed $U_c^\star$ at which the contact-line motion becomes unstable so that gas is entrained into the liquid either through bubbles forming at the cusps of a 'sawtooth' wetting line (Blake & Ruschak 1979) or by an entire film of gas being dragged into the liquid (Marchand *et al.* 2012). This is referred to as the 'maximum speed of wetting' and, in dimensionless terms, is represented by a critical capillary number $Ca_c = \mu^\star U_c^\star/\sigma^\star$. Our method for calculating Ca_c is explained in appendix A alongside benchmark calculations for its value which are compared with the results of Vandre *et al.* (2013) across a range of viscosity ratios. Excellent agreement is obtained between the results in Vandre *et al.* (2013) and those found here. As these calculations distract from the main emphasis of this work, but could be useful as a benchmark for future investigations in the field, they are provided in appendix A.

4. Effect of gas pressure on the maximum speed of wetting: analysis of a base state

Having demonstrated the accuracy of our code and shown how the critical capillary number Ca_c is calculated, we now investigate the relationship between the gas pressure $\bar{P}_g$ and Ca_c. Here, we will analyse a base state, varying only the gas pressure and A, in an attempt to deepen our understanding of the influence of non-equilibrium gas effects on the dynamic wetting process before, in § 5, performing a parametric study of the system of interest.

To ensure that we are studying an experimentally attainable regime, we use the system considered in Benkreira & Khan (2008) to provide a base state about which our parameters can be varied. In this work, a range of silicone oils of different viscosities $\mu^\star = 20$–200 mPa s are used while the density $\rho^\star = 950$ kg m^{-3}, surface tension $\sigma^\star = 20$ mN m^{-1} and equilibrium contact angle $\theta_e = 10^\circ$ remain approximately constant. Then, the characteristic (capillary) length $L^\star = 1.5$ mm and $Oh = 6 \times 10^{-3}\mu^\star$ mPa^{-1} s^{-1} depends only on the viscosity $\mu^\star$.

A base case is chosen by taking $\mu^\star = 50$ mPa s, so that $Oh_0 = 0.3$, where base state values will be denoted with a subscript 0. Taking air as the displaced fluid with $\mu_g^\star = 18$ μPa s, which remains independent of the ambient pressure (Maxwell 1867), gives a viscosity ratio of $\bar{\mu}_0 = 3.6 \times 10^{-4}$. The density of the gas $\rho_g^\star$ depends on the ambient gas pressure, with its maximum value of $\rho_g^\star = 1.2$ kg m^{-3} at atmospheric pressure

https://doi.org/10.1017/jfm.2015.121 Published online by Cambridge University Press

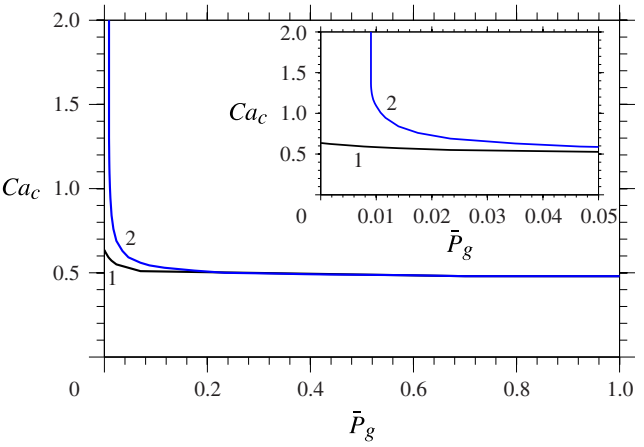

FIGURE 4. (Colour online) The dependence of the critical capillary number Ca_c on the gas pressure $\bar{P}_g$, for our base parameters: curve 1, $A = 0$ (in black); curve 2, $A = 1$ (in blue). The inset shows how curve 1 ($A = 0$) tends to a finite value of Ca_c as $\bar{P}_g \to 0$ while curve 2 appears to increase without bound.

making $\bar{\rho}_{max} = 1.3 \times 10^{-3}$. However, for all calculations performed, the value of $\bar{\rho}$ has a negligible effect on Ca_c when $\bar{\rho} \leqslant \bar{\rho}_{max}$, and so henceforth, without loss of generality, we take $\bar{\rho} = 0$, i.e. we can consider Stokes flow in the gas phase.

The slip length of the liquid–solid interface is fixed at $l_s^\star = 10$ nm, which is well within the range of experimentally observed values (Lauga *et al.* 2007), so that the dimensionless parameter $l_s = 6.8 \times 10^{-6}$. Assuming that the gas is air, we have $Kn = 4.8 \times 10^{-5}/\bar{P}_g$, so that the only parameter that remains to be specified is A, which characterises whether or not there is slip at the gas–liquid boundary.

4.1. *Effect of gas pressure*

In figure 4, the effect on Ca_c of reducing $\bar{P}_g$ is computed for $A = 0$ and $A = 1$. In each case, for $\bar{P}_g > 0.1$ there is only a slight increase in Ca_c from its value at atmospheric pressure of 0.47, which is independent of A. For $\bar{P}_g < 0.1$, dramatic changes in Ca_c are observed, whose form depends on A, so that $\bar{P}_g \approx 0.1$ appears to be the point at which non-equilibrium effects become important.

Notably, as can be seen most clearly in the inset of figure 4, for $A = 0$ as $\bar{P}_g \to 0$ we have $Ca_c \to 0.64$, whereas for $A = 1$ computations suggest that $Ca_c \to \infty$. In fact, in the latter case, once a critical pressure $\bar{P}_{g,c}$ is approached, Ca_c appears to increase without bound. For $A = 1$ this occurs at $\bar{P}_{g,c} = 9 \times 10^{-3}$; just above this value, at $\bar{P}_{g,c} = 10^{-2}$, we have $Ca_c = 1.09$, while for all $\bar{P}_g \leqslant \bar{P}_{g,c}$ we find $Ca_c > 2$.

It is impossible to show rigorously that $Ca_c \to \infty$ as $\bar{P}_g \to \bar{P}_{g,c}$ without either the computation of higher values of Ca_c, which would allow some scaling to be inferred, or, ideally, the development of an analytic framework for this problem. Unfortunately, in the former case (see § 3) computational constraints prevent us from reaching $Ca_c > 2$, while in the latter we are confined by the fact that all analytic developments, in particular those of Cox (1986), are only valid for small Ca_c. Despite this, the rapid increase of Ca_c as $\bar{P}_{g,c}$ is approached is striking, and $Ca_c = 2$ is still a large value in the context of dip-coating phenomena.

https://doi.org/10.1017/jfm.2015.121 Published online by Cambridge University Press

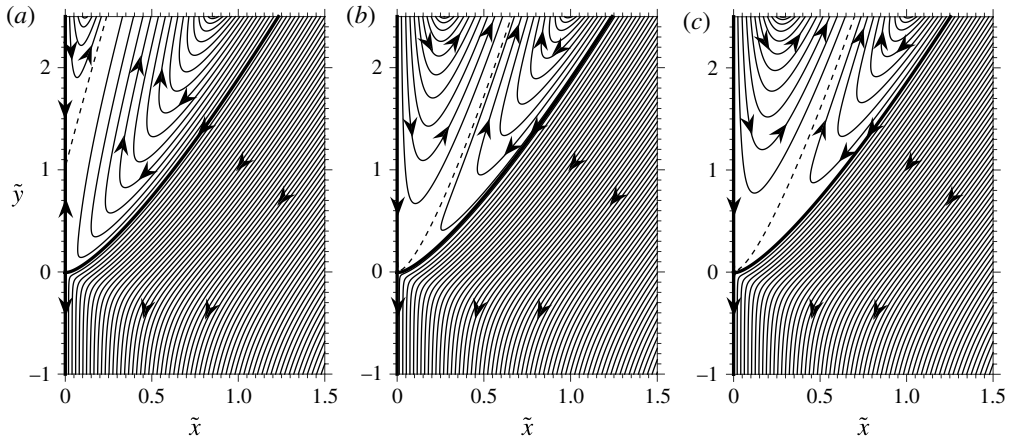

FIGURE 5. Streamlines computed at $Ca = 0.4$ for different ambient gas pressures $\bar{P}_g$ both with ($A = 1$) and without ($A = 0$) Maxwell slip at the free surface. In (*a*) $(\bar{P}_g, A) = (0.14, 0)$, (*b*) (0.14, 1) and (*c*) (0.014, 1). The local 'zoomed in' coordinates used are $\tilde{x} = x \times 10^3$ and $\tilde{y} = (y - y_c) \times 10^3$, where y_c is the contact-line position, and streamlines emanate from equally spaced points across $\tilde{y} = 2.5$ with the dividing streamline dashed.

To summarise, it has been shown that when Maxwell slip is accounted for on both the gas–solid and gas–liquid interfaces the maximum speed of wetting appears to be unbounded as the ambient pressure is reduced, whereas if slip on the latter surface is neglected ($A = 0$), the maximum speed remains finite. In other words, the error associated with neglecting Maxwell slip on the free surface is extremely large at reduced pressures and appears to be infinite in the limit $\bar{P}_g \to 0$.

4.2. *Flow kinematics*

In figure 5, streamlines of the flow near the contact line are shown at $Ca = 0.4$ in three different regimes: (*a*) at a pressure where non-equilibrium effects are weak, $\bar{P}_g = 0.14$ with $A = 0$, (*b*) $\bar{P}_g = 0.14$ with $A = 1$ and (*c*) at a pressure where non-equilibrium effects are becoming influential, $\bar{P}_g = 0.014$ with $A = 1$. Given that $L^\star \sim 1$ mm for typical liquids, dimensionally the scale in figure 5 is a few microns. In all cases, the flow of the liquid, which is below the free surface (represented by a thick black line), remains virtually unchanged, with the motion of the solid, located at $\tilde{x} = 0$, dragging liquid downwards which, to conserve mass, is continually replenished from above. If one notes that the free surface meets the solid at an equilibrium contact angle of 10°, and yet any apparent angle defined on the scale seen in figure 5 would be obtuse, it is clear that at this relatively high capillary number there is significant deformation of the free surface on a scale below what is visible here.

In all three cases, the flow of liquid, which seems immune to the gas dynamics, results in an almost identical velocity tangential to the free surface on the liquid-facing side of this interface, as shown from curves 1a, 2a, 3a in figure 6(*a*), where the velocities tangential to the gas–solid and liquid–gas interfaces have been plotted.

At the top, $\tilde{y} = 2.5$, of the figures, the gas flow field is qualitatively similar in all cases. The motion of both the liquid and the solid drives gas towards the contact-line region which, to ensure continuity of mass, results in a 'split ejection' type flow, as observed in immiscible liquid–liquid systems (Dussan V & Davis 1974; Dussan V

https://doi.org/10.1017/jfm.2015.121 Published online by Cambridge University Press

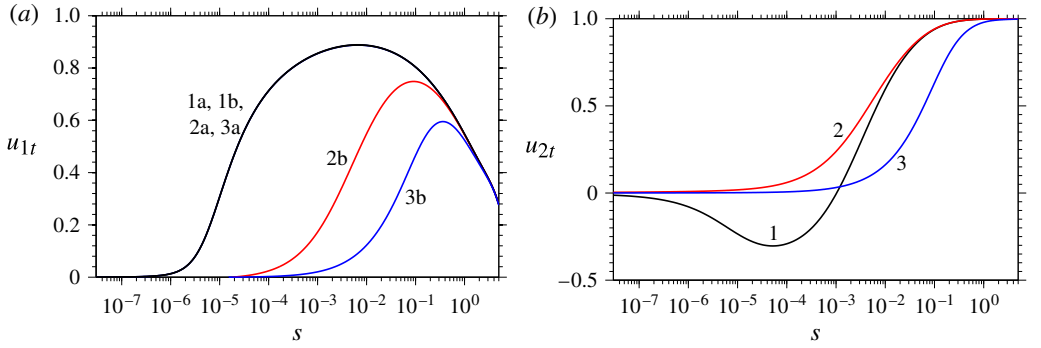

FIGURE 6. (Colour online) Tangential velocities as a function of distance from the contact line s along (a) the liquid–gas and (b) the gas–solid boundary computed at $Ca = 0.4$: curve 1, $(\bar{P}_g, A) = (0.14, 0)$; curve 2, (0.14, 1); curve 3, (0.014, 1). The velocity tangential to the free surface and pointing towards the contact line is u_{1t}, with designation a for the liquid-facing side of the interface and b for the gas side. The tangential velocity on the gas–solid interface pointing towards the contact line is u_{2t} and the speed of the solid is 1.

1977), with an upwards flux of gas through the middle of this domain. For $A = 1$ the split ejection flow is maintained right up to the contact line (figure 5*b*,*c*); however, for $A = 0$ a flow reversal occurs on the solid–gas interface at $\tilde{y} \approx 1$ so that the direction of the gas flow actually opposes that of the solid for $\tilde{y} < 1$ (figure 5*a*). The flow reversal can clearly be seen from curve 1 in figure 6(*b*) for $s < 10^{-3}$, with a substantial minimum of $u_{2t} = -0.3$, and can also be seen in previous works, such as figure 10(*b*) of Vandre *et al.* (2013).

The asymmetric gas flow observed for $A = 0$ appears because in this case the gas velocity is continuous across the liquid–gas free surface, see curves 1a and 1b in figure 6(*a*), but is allowed to slip across the solid boundary according to Maxwell's condition, see curve 1 in figure 6(*b*). This results in the liquid driving a gas flow towards the contact line which, when combined with the requirement of mass conservation, leads to such a large increase of tangential stress at the solid, that the slip across the interface, determined by (2.4*b*), is sufficient to reverse the flow direction. This effect will be further considered, in a lubrication setting, in § 4.4.

When $A = 1$, slip is also allowed at the gas–liquid interface, see curves 2a and 2b in figure 6(*a*), so that, as can be seen from curve 2 in figure 6(*b*), there is no flow reversal on either of the boundaries of the gas. This more symmetric flow field remains when the gas pressure is decreased to $\bar{P}_g = 0.014$, see figure 5(*c*) and the curves labelled 3 in figure 6. Although the flow remains qualitatively the same, one can clearly see from figure 6 that lowering the pressure significantly increases slip at the gas boundaries. For example, at $s = 10^{-2}$, for $\bar{P}_g = 0.14$ the velocity on the solid $u_{2t} = 0.65$, whereas for $\bar{P}_g = 0.014$ the velocity is just $u_{2t} = 0.16$. Therefore, less gas is dragged into the contact-line region when (a) slip is accounted for on the gas–liquid boundary ($A = 1$) and/or (b) slip is increased through reductions in pressure. Both of these mechanisms reduce the resistance of the gas to contact-line motion, as shown analytically in § 4.4, and contribute to postponing the point of wetting failure.

4.3. *Characteristics of the gas film*

At high capillary numbers there is a region between the contact line and the far field in which the gas domain is a 'thin film'. This region is sufficiently far from the

https://doi.org/10.1017/jfm.2015.121 Published online by Cambridge University Press

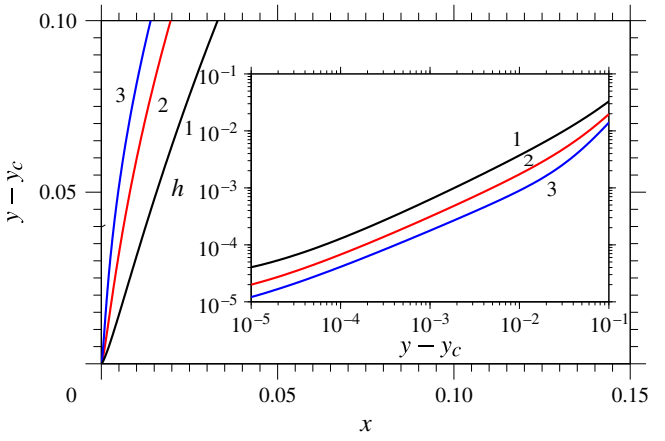

FIGURE 7. (Colour online) Free-surface shapes obtained in our base case, with $\bar{P}_g = 0.014$ and $A = 1$: curve 1, $Ca = 0.4$ (in black); curve 2, $Ca = 0.6$ (in red); curve 3, $Ca = 0.8$ (in blue). The inset shows how the height of the gas film h varies as a function of $y - y_c$, showing that for $10^{-4} < y - y_c < 10^{-1}$ it can be considered in a lubrication setting.

contact-line region where the free surface bends from its equilibrium angle of 10° towards an obtuse apparent angle and near enough to the contact line that gravitational forces have not started to flatten the free surface. For our base case, for $Ca \geqslant 0.4$, which includes all values of Ca_c, this region exists in the range $10^{-4} < y - y_c < 10^{-1}$, as one can see from figure 7. Specifically, the main figure clearly shows that the gas film is 'thin' on the scale of approximately $y - y_c \sim 0.1$, while the inset shows on a logarithmic plot that this behaviour continues down to $y - y_c \sim 10^{-4}$.

The dynamics of the gas film is key to the air entrainment phenomenon, so that one may expect that reductions in ambient pressure will only start to influence Ca_c once Maxwell slip on the boundaries is large enough to affect the gas flow characteristics. This occurs when the (dimensionless) slip length $Kn = 4.8 \times 10^{-5}/\bar{P}_g$ becomes comparable with the height of the gas film $x = h(y)$. This results in a function $Kn_{loc}(h) = Kn/h$ which characterises the importance of non-equilibrium effects as one goes along the film. How though should we define a particular position along the film $h = H$ on which we can base a local Knudsen number Kn_H?

Research into dynamic wetting/dewetting phenomena (Dejaguin & Levi 1964; Eggers 2004; Vandre *et al.* 2013) has long recognised that wetting failure is strongly linked to the behaviour of the inflection point on the free surface, where the curvature of the surface changes sign; this point can also be used to define an apparent contact angle (Tanner 1979). Given that the flow near the inflection point seems to be key to determining Ca_c, this point is a sensible choice for defining the characteristic film height H, see figure 2. To do so, we must extract H from our computations and determine how it depends on Ca and $\bar{P}_g$.

In figure 8, we can see that although Ca_c depends on $\bar{P}_g$, the value of H is approximately independent of $\bar{P}_g$, so that $H \approx H(Ca)$, with smaller $\bar{P}_g$ simply revealing more of this curve. In fact, a similar curve is obtained if the gas flow is ignored altogether ($\bar{\mu} = 0$), as shown by the dashed line in figure 8, although this may not be the case at higher viscosity ratios. Notably, H decreases rapidly with increasing Ca in agreement with previous experiments (Marchand *et al.* 2012) and simulations (Vandre *et al.* 2013). Reassuringly, at $Ca = Ca_c$ the film height obtained at atmospheric

https://doi.org/10.1017/jfm.2015.121 Published online by Cambridge University Press

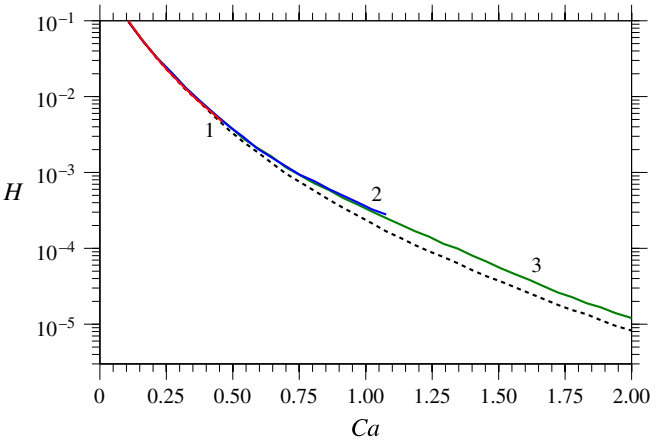

FIGURE 8. (Colour online) The dependence of the gas film height H, at the inflection point on the free surface, on the capillary number Ca. The curve is largely independent of gas pressure $\bar{P}_g$, although lower values of $\bar{P}_g$ allow more of the curve to be obtained. The curves correspond to 1, $\bar{P}_g = 1$ (red); 2, $\bar{P}_g = 10^{-2}$ (blue); 3, $\bar{P}_g = 9 \times 10^{-3}$ (green); the dashed line is obtained for $\bar{\mu} = 0$.

ΔCa_c (%)	$\bar{P}_g$	H	Kn_H
0	1	4.2×10^{-3}	0.011
10	0.16	3.1×10^{-3}	0.1
20	7×10^{-2}	2.3×10^{-3}	0.3
50	2.3×10^{-2}	1.1×10^{-3}	1.9
100	1.2×10^{-2}	4.1×10^{-4}	9.8
$\geqslant 300$	$\leqslant 9 \times 10^{-3}$	$\leqslant 7.1 \times 10^{-5}$	$\geqslant 75$

TABLE 1. The pressure reduction $\bar{P}_g$ required for a given enhancement in capillary number ΔCa_c with the corresponding film height H and Knudsen number at the inflection point Kn_H at this pressure.

pressure, $H = 4.2 \times 10^{-3}$, dimensionally corresponds to a film $H^\star = 1$–10 μm for typical liquids, which is precisely what has been found experimentally in Marchand *et al.* (2012).

Enhancements in Ca_c at reduced pressure can be quantified by the percentage increase in Ca_c from its atmospheric value $Ca_{c,atm}$, defined by $\Delta Ca_c = 100(Ca_c - Ca_{c,atm})/Ca_{c,atm}$, which is given in table 1. As well as listing the pressure reduction required, values for H are given from which $Kn_H = Kn/H$ is calculated. The data show that $\bar{P}_g \sim 0.1$, where significant increases in ΔCa_c begin, corresponds to $Kn_H \sim 0.1$. Therefore, non-equilibrium effects in the gas, which manifest themselves through Maxwell slip, alter the flow once the slip length is approximately 10 % of the gas film characteristic height, and it is this mechanism that determines when variations in $\bar{P}_g$ can start to affect Ca_c.

Notably, all inflection points calculated in table 1 fall into the thin-film region apart from the entries where the critical gas pressure has been passed, after which the inflection point gets close to the region of high curvature near the contact line. This suggests that the critical pressure $\bar{P}_{g,c} = 9 \times 10^{-3}$ could be the value at which the

https://doi.org/10.1017/jfm.2015.121 Published online by Cambridge University Press

inflection point is no longer located in the thin-film region. From table 1 we can see that for $\bar{P}_g \leqslant \bar{P}_{g,c}$ we have $Kn_H \geqslant 75$, so that Maxwell slip is so strong that the gas flow is hardly affected by the motion of its boundaries. In this case, the gas effectively offers no resistance to the dynamic wetting process and Ca_c is able to increase without bound.

4.3.1. *Limitations of the Maxwell-slip model*

From table 1 it is clear that the combined increases in Kn and decreases in H at reduced pressures both contribute to rapid changes in Kn_H. Across a reduction in the gas pressure of $\sim 10^2$, Kn_H increases from its atmospheric value by a factor of $\sim 10^4$. Consequently, many values of Kn_H in the table fall well outside the 'slip regime' where non-equilibrium effects can be attributed entirely to the boundary conditions. Therefore, attribution of non-equilibrium effects entirely to the boundary conditions, via Maxwell slip, as has been considered here, is not sufficient to accurately capture its behaviour. This calls into question a number of the results that have been obtained with a gas model that goes outside its strict limits of applicability for the smaller values of $\bar{P}_g$. In particular, is it likely that the behaviour $Ca_c \to \infty$ as $\bar{P}_g \to \bar{P}_{g,c}$, or even as $\bar{P}_g \to 0$, remains robust?

To address this question we must understand more about the Knudsen layer in regimes where its effects can no longer be attributed entirely to the boundary conditions. A useful result for this phenomenon has been obtained in Lockerby, Reese & Gallis (2005*b*) for pressure-driven Poiseuille flow in a channel. There, it was shown that at a Knudsen number of just $Kn = 0.025$, the increased mass flow rate above that obtained for no-slip is approximately 70 % due to increased slip at the wall, while 30 % is due to non-Newtonian effects in the Knudsen layer. This latter phenomenon is not accounted for in our work and suggests that the incorporation of more complex gas dynamics is likely to enhance the effects already observed with Maxwell slip rather than suppress them. Therefore, there is good reason to believe that with the incorporation of more complex gas models the qualitative trends observed for Ca_c will remain, while quantitatively its value could increase for a given $\bar{P}_g$.

We shall return to these points in more detail in § 8; however, in what follows we will continue to use the problem formulation outlined in § 2 to give insight into the role that non-equilibrium effects play in the gas, despite, in some cases, the model being outside its strict region of applicability.

4.4. *Lubrication analysis*

Given the importance of the gas film behaviour, it is of interest to see whether analytic progress in a lubrication setting will shed some light on the dynamics of this film. Figure 6(*a*) shows that u_{1t}, the liquid velocity tangential to the free surface, is within 10 % of $u_{1t} = 0.85$ throughout the thin-film region. This is a useful observation, as it allows us to make analytic progress by assuming that the liquid approximately provides a constant downward velocity $V = 0.85$ along the free surface in this region.

In the lubrication setting, the steady gas flow between two impermeable surfaces, at $x = 0$ and $x = h$, generated by their velocities of magnitude, respectively, $v = -1$ and $v = -V$, will, in order to conserve mass ($\int_0^h v \mathrm{d}x = 0$), have parabolic form $v = a(x^2 - h^2/3) + b(x - h/2)$. The coefficients a, b are obtained by applying the boundary conditions at $x = 0, h$ which are, respectively, the Maxwell-slip equations (2.4*a*,*b*) and

https://doi.org/10.1017/jfm.2015.121 Published online by Cambridge University Press

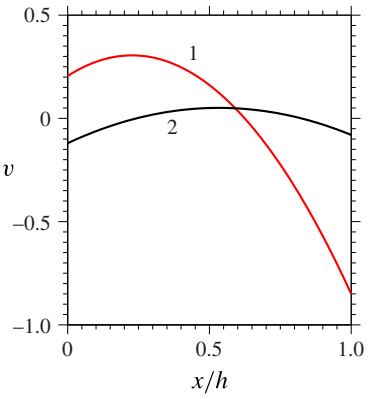

FIGURE 9. (Colour online) Vertical velocity v predicted by the lubrication analysis for $h = 2.5 \times 10^{-4}$ at $\bar{P}_g = 0.14$ for the cases of $A = 0$, curve 1 in red, and $A = 1$, curve 2 in black. One can see that when $A = 0$ the lubrication analysis predicts the flow reversal at $x = 0$, while this does not occur for $A = 1$. These results can be compared with those in figure 5(*a*,*b*) by looking at $\tilde{y} = 0.3$ where $h = 2.5 \times 10^{-4}$.

(2.7). Introducing $Kn_{loc} = Kn/h$, the result is

$$a = \frac{-3\left[1 + 2AKn_{loc} + V\left(2Kn_{loc} + 1\right)\right]}{h^2\left[1 + 4Kn_{loc}(1 + A) + 12AKn_{loc}^2\right]} \quad \text{and} \quad b = \frac{2(3 - ah^2)}{3h\left(2Kn_{loc} + 1\right)}. \tag{4.1a,b}$$

A good test for the lubrication theory is to see whether it is able to predict the flow reversal at the solid surface observed in figure 5(*a*) for the case of $A = 0$. To do so requires that $v(x = 0) > 0$, which for $A = 0$ can be shown to occur when $Kn_{loc} > 1/(2V)$, so that flow reversal is indeed possible if Kn_{loc} is sufficiently large. For the case in figure 5(*a*), using $V = 0.85$ and $Kn_{loc} = 3.4 \times 10^{-4}/h$, the lubrication analysis predicts flow reversal for $h < h_r = 5.8 \times 10^{-4}$, with a typical flow profile in this regime shown by curve 1 in figure 9. The agreement with the computed value of $h_r = 6.2 \times 10^{-4}$ is good and is an indication of the accuracy of our approximations in this region.

For $A = 1$, where there is slip on each interface, we find that for $V < 1$, which is always satisfied, there are no real roots for Kn_{loc}, so that $v(x = 0) < 0$ for all h. In other words, in this case there is no flow reversal adjacent to the solid, in agreement with the streamlines shown in figure 5(*b*,*c*). The accuracy of the lubrication approximation for this flow is confirmed in figure 10, where the computed velocity tangential to the gas boundaries u_t is plotted against the vertical velocity predicted by (4.1). It should be noted that here, we have used the computed value of V at the free surface, to enable a more accurate assessment of the lubrication approximation, rather than the estimate $V = 0.85$ used elsewhere.

In Vandre *et al.* (2013), it is shown that air entrainment occurs when the capillary forces at the inflection point cannot sustain the pressure gradients required to remove gas from the lubricating gas film. Here, the pressure gradient Δp required to maintain the flow at the inflection point, where $Kn_{loc}(h = H) = Kn_H$, is given by

$$\Delta p \equiv \left.\frac{\partial p}{\partial y}\right|_{h=H} = \bar{\mu}\left.\frac{\partial^2 v}{\partial x^2}\right|_{h=H} = -\frac{6\bar{\mu}\left[1 + 2AKn_H + V\left(2Kn_H + 1\right)\right]}{H^2\left[1 + 4Kn_H(1 + A) + 12AKn_H^2\right]}. \tag{4.2}$$

https://doi.org/10.1017/jfm.2015.121 Published online by Cambridge University Press

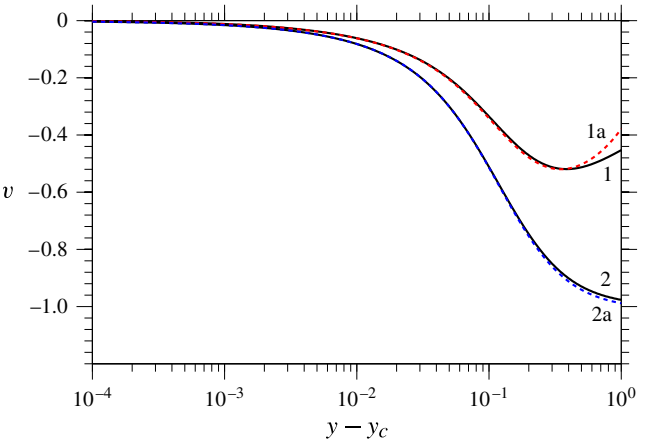

FIGURE 10. (Colour online) Comparison of the computed gas velocity tangential to the boundaries of the gas with the vertical velocity from the lubrication analysis for the case of $A = 1$ and $\bar{P}_g = 0.014$. Curves 1 and 2 are, respectively, computed values along the free surface and the solid surface, while the corresponding curves from the lubrication analysis are 1a in red and 2a in blue. Notably, there is no flow reversal as $v \leqslant 0$ in all cases.

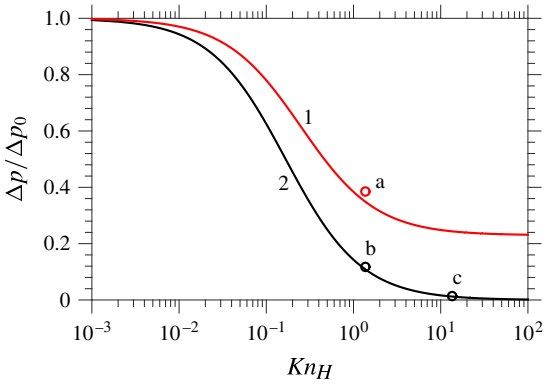

FIGURE 11. (Colour online) Normalised pressure gradient $\Delta p/\Delta p_0$ given as a function of Kn_H: curve 1, $A = 0$ (in red); curve 2, $A = 1$ (in black). The circles labelled a, b and c are the values computed for the pressure gradient at $\tilde{y} = 0.3$ for the cases shown in figure 5(*a–c*), and these compare well with the predictions of the lubrication analysis.

As $Kn_H \to 0$, so that one approaches no-slip on the solid surface, we have $\Delta p \to \Delta p_0 = -6\bar{\mu}(1 + V)/H^2$, and in figure 11 the pressure gradient in (4.2), normalised by Δp_0, is given as a function of Kn_H for the cases of $A = 0, 1$ and shown to agree well with the values from our computations. Notably, curves 1, 2 for $A = 0, 1$ show that for large Kn_H the normalised pressure gradient for $A = 0$ asymptotes towards a non-zero value while for $A = 1$ it tends to zero. Determination of $\Delta p/\Delta p_0$ as $Kn_H \to \infty$ from (4.2) confirms that for $A = 0$ the limit is finite at $V/(2(1 + V)) = 0.23$, while for $A = 1$ the limit is zero.

These findings help us to understand the results shown in figure 4. For $A = 1$, as the ambient pressure is reduced ($\bar{P}_g \to 0$), and hence Maxwell slip is increased ($Kn_H \to \infty$), the pressure gradient required to pump gas from the contact-line region

https://doi.org/10.1017/jfm.2015.121 Published online by Cambridge University Press

vanishes, so that the gas offers no resistance to contact-line motion and, consequently, the maximum speed of wetting appears to become unbounded, $Ca_c \to \infty$. In contrast, for $A = 0$, the lack of slip at the free surface means that gas is always being driven into the contact-line region by the motion of the liquid so that however much $\bar{P}_g$ is reduced (Kn_H increased) a pressure gradient in the gas is always required and Ca_c approaches a finite value based on this.

4.5. *Evaluation of the incompressibility assumption*

The analytic expression derived for the pressure gradient in the thin film (4.2) can be used to estimate the validity of the assumptions we have made about the gas flow. In particular, although the flow is clearly low Mach number, compressibility effects in thin films can still be significant, see § 4.5 of Gad-el-Hak (2006). This occurs when the large pressure gradients required to pump gas out of the thin film lead to reductions in pressure that are comparable with the ambient pressure in the gas. As it is the gas flow at the inflection point on the free surface that is most important for air entrainment, we will estimate whether the flow in the gas there is indeed incompressible.

The pressure gradient obtained in (4.2) takes a maximum value of $\Delta p_0 = -12\bar{\mu}/H^2$, as $V \leqslant 1$, so that the maximum pressure change along a film of length L_f is $12\bar{\mu}L_f/H^2$. Simulations show that the film length is never larger than the capillary length, so that $L_f = 1$ is an upper bound. Comparison of the pressure change with the (dimensionless) ambient pressure P_g, which is $P_g = P_g^\star L^\star/(\mu^\star U^\star)$, gives us that compressibility can be neglected if $\Delta p_0 \ll P_g$, which requires

$$H \gg H_T = 3.5\sqrt{\mu_g^\star U^\star/(P_g^\star L^\star)}, \tag{4.3}$$

where H_T is the (dimensionless) transition height below which compressible effects can no longer be neglected. This is consistent with a similar condition derived for drop impact phenomena in Mani *et al.* (2010).

Taking $U^\star = 1$ m s^{-1} gives $H_T = 1.2 \times 10^{-3}$ for air at atmospheric pressure, while reducing the pressure by a factor of one hundred gives $H_T = 1.2 \times 10^{-2}$. When looking at the values of H obtained at various Ca in figure 8 it appears that compressibility may indeed be important. However, the estimate obtained in (4.3) overpredicts H_T due to (*a*) neglecting reductions in pressure gradients associated with slip at the interfaces and (*b*) approximating the film as being a channel of length L and constant height H, whereas the film height actually increases by orders of magnitude as one moves away from the contact line, see figure 7. Therefore, before abandoning incompressibility, a more accurate evaluation of this assumption is considered in which the pressure changes along the film obtained from our computations are used instead of Δp_0 from (4.2).

In figure 12 the variation in p_g from its far-field value p_f is plotted as a function of distance from the contact line $y - y_c$, along both the gas–solid and gas–liquid interfaces for the cases shown in figure 5(*b*,*c*), i.e. for $\bar{P}_g = 0.14, 0.014$ with $A = 1$. As one would expect in a lubrication flow, the values along the two interfaces are close and are graphically indistinguishable along curve 2. It can be seen that the maximum change in p_g in the thin-film region for the cases considered is 17 and 3 respectively. For the liquid associated with the base state, the substrate speed at $Ca = 0.4$ is $U^\star = 0.16$ m s^{-1}, so that for $\bar{P}_g = 0.014$, where the gas is most likely to be compressible, we have $P_g = 260$. Therefore, in these cases the pressure change

https://doi.org/10.1017/jfm.2015.121 Published online by Cambridge University Press

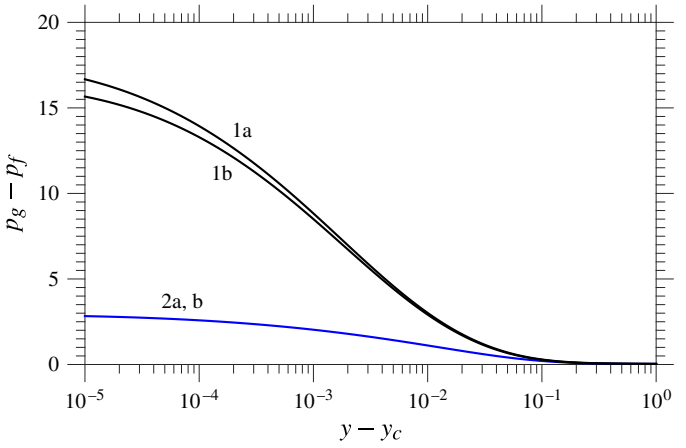

FIGURE 12. (Colour online) Deviation of the gas pressure p_g from its far-field value of p_f as a function of distance from the contact line $y - y_c$, with curves 1 (in black) and 2 (in blue) corresponding to, respectively, the cases considered in figure 5(*b*,*c*). The pressure along the gas–solid interface is given by curves 1a, 2a, while 1b, 2b are values from the gas–liquid interface.

along the film $p_g - p_f$ is substantially smaller than the ambient pressure P_g, with $(p_g - p_f)/P_g < 0.012$.

Notably, although the lubrication analysis accurately predicts the pressure gradient in the film, see figure 11, use of the analytic value at the inflection point to estimate the pressure change along the entire length of the thin film is inaccurate. This is due to the widening of the film as one moves away from the contact line. A more accurate estimate could have been achieved by integrating the analytically calculated pressure gradient over the computationally obtained film profile, but a simpler way is to use the computed values of p_g. Doing this shows that the assumption of incompressibility is an accurate one for the base cases considered. Further simulations confirm that even in the most extreme cases considered here, the incompressibility assumption remains a good one.

5. Parametric study of the system

Having fully analysed the base state, the role of the system parameters is now established by perturbing their values about the base ones. Henceforth, we only consider the most physically relevant case of $A = 1$.

5.1. *Influence of viscosity ratio*

The viscosity ratio $\bar{\mu}$ has long been recognised as an important parameter in coating flows as it is a measure of how much resistance the receding gas phase can produce. Working with a dimensionless system allows us to isolate the effect of $\bar{\mu}$ on Ca_c, at different ambient pressures, while keeping all other parameters fixed at their base state. The range considered is chosen to cover all values of $\bar{\mu}$ obtained for the liquids in Benkreira & Khan (2008) used to coat a solid in air, giving $10^{-4} \leqslant \bar{\mu} \leqslant 10^{-2}$.

In figure 13 one can see that lower values of the viscosity ratio $\bar{\mu}$ result in higher Ca_c across all values of $\bar{P}_g$. What was less expected is that for $\bar{P}_g = 0.01$ (curve 3)

https://doi.org/10.1017/jfm.2015.121 Published online by Cambridge University Press

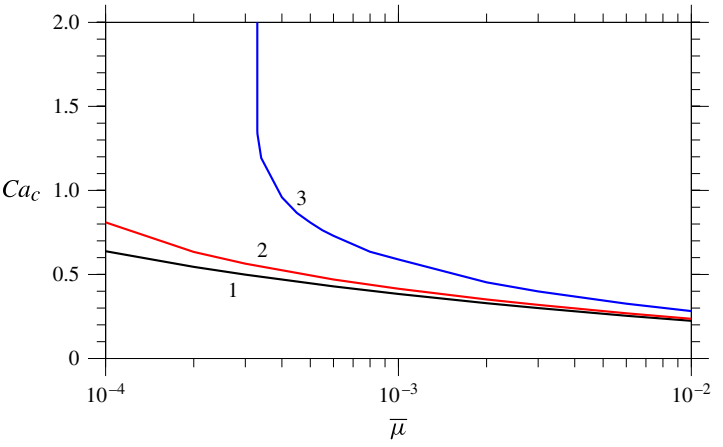

FIGURE 13. (Colour online) Dependence of the critical capillary number Ca_c on the viscosity ratio $\bar{\mu}$, with all other parameters fixed at their base values: curve 1, $\bar{P}_g = 1$ (black); curve 2, $\bar{P}_g = 0.1$ (red); curve 3, $\bar{P}_g = 0.01$ (blue).

it appears that there is a value of $\bar{\mu}$ below which Ca_c increases apparently without bound. This occurs at $\bar{\mu} = 3.3 \times 10^{-4}$, which is slightly less than the base case viscosity ratio ($\bar{\mu}_0 = 3.6 \times 10^{-4}$) where the critical gas pressure $P_{g,c} = 9 \times 10^{-3}$. Therefore, at smaller $\bar{\mu}$ the critical value $\bar{P}_{g,c}$ increases, i.e. less pressure reduction is required to reach the critical value.

The effect of $\bar{\mu}$ on $\bar{P}_{g,c}$ can be understood by looking back to the lubrication analysis in the previous section and, in particular, the expression for the pressure gradient in the gas (4.2), which is proportional to $\bar{\mu}$ (in dimensional terms it would be proportional to $\mu_g^\star$). Therefore, while the degree of Maxwell slip controls the boundary conditions to the gas flow, the bulk flow in the gas is characterised by the viscosity ratio $\bar{\mu}$, with larger values decreasing Ca_c as more effort is required to remove gas from the contact-line region.

5.2. *Effect of Ohnesorge number*

The effects of inertia are usually assumed to have a negligible influence on the dynamics of air entrainment, with Stokes flow, corresponding to $Oh \to \infty$, often considered. In full computations of coating flows in Vandre *et al.* (2013) it was shown that (*a*) inertial effects in the gas have a negligible influence, reaffirming our assumption that $\bar{\rho} = 0$ can be taken without loss of generality, and (*b*) inertial forces in the liquid do not alter Ca_c until they are relatively large. The results in figure 14 at atmospheric pressure agree with these previous conclusions, with a 10^2 reduction in Oh only increasing the value of Ca_c by approximately 10 %. It should be noted that Ca_c at $Oh = 0.1$ corresponds to $Re = 52$.

For the lowest ambient pressure $\bar{P}_g = 0.01$ an entirely different behaviour is observed and there is a critical value of Oh where Ca_c appears to increase without bound. In contrast to the influences of $\bar{P}_g$ and $\bar{\mu}$ which could be rationalised by considering the gas flow, this effect is generated by changes in the liquid dynamics. In particular, in Vandre *et al.* (2013) it was shown that when inertial effects become more prominent, velocity gradients in the liquid are localised to a thin boundary layer near the moving solid surface and, as a result, the free surface becomes less

https://doi.org/10.1017/jfm.2015.121 Published online by Cambridge University Press

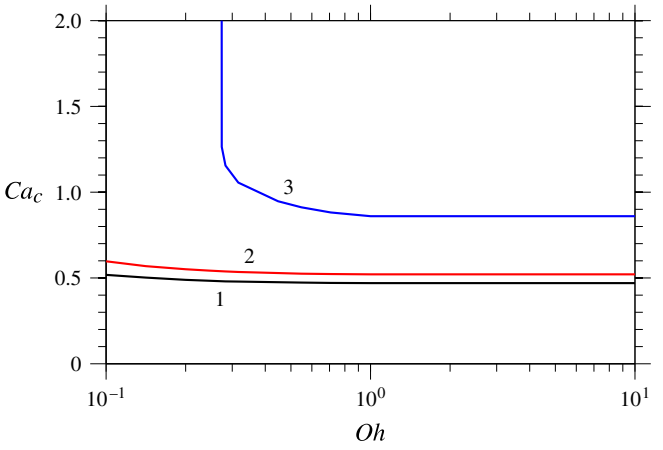

FIGURE 14. (Colour online) The dependence of the critical capillary number Ca_c on the Ohnesorge number Oh with all other parameters fixed at their base values: curve 1, $\bar{P}_g = 1$ (black); curve 2, $\bar{P}_g = 0.1$ (red); curve 3, $\bar{P}_g = 0.01$ (blue).

deformed so that Ca_c increases. Our results show that when combined with small values of $\bar{P}_g$ this mechanism can prevent air entrainment at any Ca.

5.3. *Role of substrate wettability*

Experimentally, the wettability of the substrate is known to have an influence on the point of air entrainment both in coating flows and in impact problems, such as the impact of solid spheres on liquid baths (Duez *et al.* 2007). In figure 15, our results obtained at constant contact angles $\theta_d = \theta_e$, show that the more wettable the substrate, the higher Ca_c is. The curves are from $5^\circ \leqslant \theta_e \leqslant 175^\circ$ to avoid computational difficulties associated with extremely small angles in either phase, but, despite this, the trends are still clear enough. Notably, at reduced pressures variations in Ca_c with θ_e are far more dramatic: changing θ_e from 30° to 90° reduces Ca_c by 0.32 at $\bar{P}_g = 0.01$ compared with 0.1 at $\bar{P}_g = 1$.

The model used here predicts that Ca_c monotonically decreases as θ_e increases, which is what one may intuitively expect. However, in Blake & De Coninck (2002) the optimal value of θ_e that maximises Ca_c is not at zero and can even occurs on hydrophobic substrates, $\theta_e \geqslant 90^\circ$. It is likely that such effects can only be captured by using a dynamic contact angle model and so this aspect lies beyond the scope of the present paper. However, further experiments at both atmospheric and reduced pressure for solids of different wettabilities would be useful to shed further light on these issues.

5.4. *Different gases*

Previous studies in both dip coating (Benkreira & Ikin 2010) and drop impact (Xu *et al.* 2005) have considered the effect of using different gases on wetting failure. The gases used tend to have a similar viscosity and density at atmospheric pressure to air but possess different molecular weights and hence mean free paths. The fluid flow considered here is incompressible, so that changes in the speed of sound in the gas, and hence the Mach number, do not concern us. However, changes in the mean free

https://doi.org/10.1017/jfm.2015.121 Published online by Cambridge University Press

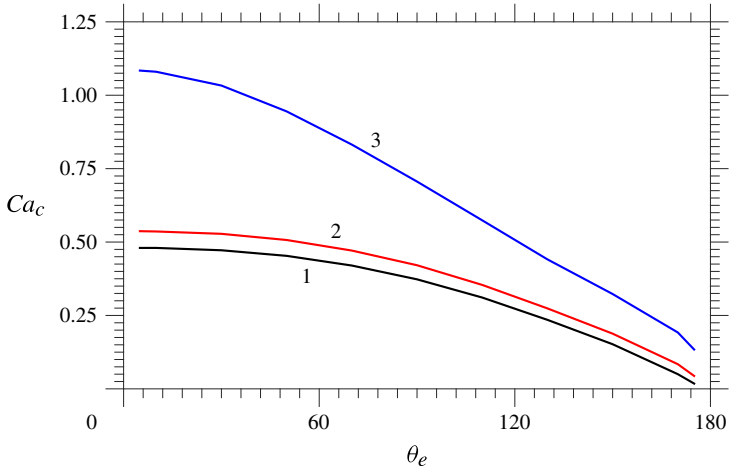

FIGURE 15. (Colour online) The dependence of the critical capillary number Ca_c on the equilibrium contact angle θ_e with all other parameters fixed at their base values: curve 1, $\bar{P}_g = 1$ (black); curve 2, $\bar{P}_g = 0.1$ (red); curve 3, $\bar{P}_g = 0.01$ (blue).

path at a given ambient pressure will have an effect on our results. This effect can be accounted for in the results presented, without recomputing everything, by simply rescaling the ambient gas pressure $\bar{P}_g$. For example, if a new gas considered has a mean free path $\ell^\star_{atm,n}$ that is c times larger than that of air at atmospheric pressure, so that $\ell^\star_{atm,n} = c\ell^\star_{atm}$, then from (1.4) the same Kn is obtained if we use a rescaled pressure $\bar{P}_{g,n}$ in the new gas that satisfies $\bar{P}_{g,n} = c\bar{P}_g$.

In this way, all the results of the previous section can be used for any gas, rather than just air. For example, if helium is used instead of air, approximately $\ell^\star_{atm,\mathrm{He}} = 3\ell^\star_{atm,air}$, so that $\bar{P}_{g,\mathrm{He}} = 3\bar{P}_g$. Then, for the base case considered in § 4.1 the critical pressure was found to be $\bar{P}_g = 9 \times 10^{-3}$ for air so that for helium this would be increased to $\bar{P}_g = 2.7 \times 10^{-2}$. Therefore, as seen experimentally, built into the model is the fact that gases with larger mean free paths require less pressure reduction in order to induce significant non-equilibrium gas effects that increase Ca_c.

5.5. *Summary of the parametric study*

The effects of non-equilibrium gas dynamics on air entrainment phenomena have been clarified and the role of the various dimensionless parameters on Ca_c has been characterised by perturbing them about a base case. This has allowed us to isolate the effects of parameters such as $\bar{\mu}$ which cannot easily be independently varied experimentally. The disadvantage is, of course, that the results cannot easily be used to find, say, the effect of $\mu^\star$ on coating speeds, as this variable comes into Ca, Oh and $\bar{\mu}$, which have thus far been varied independently. Therefore, in the next section we compare our results directly with experiments in Benkreira & Khan (2008) and, in doing so, now step into a dimensional setting.

6. Comparison with experimental data: effect of viscosity and gas pressure

We consider now whether the new model is able to account for the influence of the gas pressure $P^\star_g$ on the maximum coating speeds $U^\star_c$ observed in Benkreira &

https://doi.org/10.1017/jfm.2015.121 Published online by Cambridge University Press

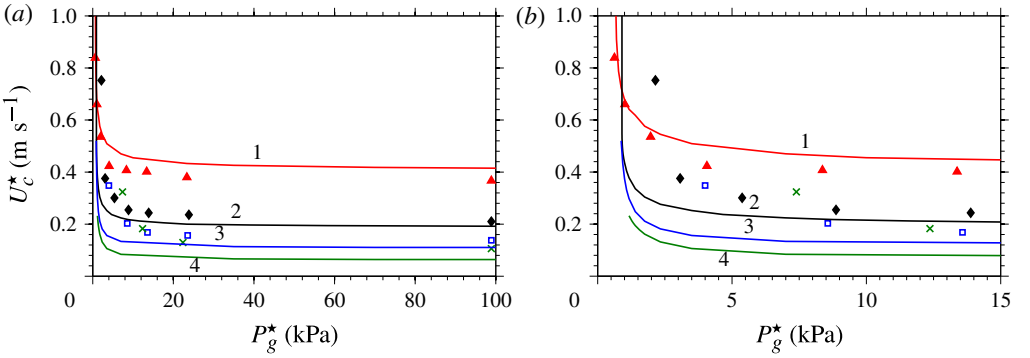

FIGURE 16. (Colour online) A comparison of our computations for the critical wetting speed $U_c^\star$ as a function of the gas pressure $P_g^\star$ with experimental results obtained in Benkreira & Khan (2008). Curves are computed for liquids of different viscosities $\mu^\star$: curve 1, 20 mPa s (in red); curve 2, 50 mPa s (in black); curve 3, 100 mPa s (in blue); curve 4, 200 mPa s (in green). The corresponding experimental data are given by, respectively, triangles, diamonds, squares and crosses.

Khan (2008) for different viscosity liquids. All parameters remain unchanged from § 5 except for those that depend on viscosity, namely Oh, Ca and $\bar{\mu}$, which will be based on values used in the experiments of $\mu^\star = 20$, 50, 100, 200 mPa s.

In figure 16, a direct comparison between the computations and the experimental results in Benkreira & Khan (2008) is shown. Notably, both predict that a significant reduction in $P_g^\star$ from its atmospheric value ($P_{g,atm}^\star = 100$ kPa) is required to induce increases in $U_c^\star$, but that once this has been achieved, the subsequent enhancements in $U_c^\star$ are substantial. At the lowest viscosity, the agreement is relatively good throughout; however, as is most clear from figure 16(*b*), one can see that at the higher viscosities, the effect of gas pressure yields enhanced coating speeds earlier in the experiments than in the computations. For example, for the highest viscosity liquid, at $P_g^\star = 12$ kPa the experimental data (crosses) show that $U_c^\star$ has increased to 0.18 m s^{-1} from its atmospheric value of 0.11 m s^{-1}, while the computations, shown by curve 4, only give this degree of enhancement once $P_g^\star = 2$ kPa.

Promisingly, as in the experimental results, curves 1 and 2 cross at low atmospheric pressure, meaning that a higher-viscosity liquid can be coated at faster speeds than a lower one, in contrast to what is observed at atmospheric pressure. Other crossovers may have been observed if higher capillary numbers could have been obtained, as suggested by the path of curve 3. However, the positions of the crossovers do not match the experimental data; while the computed results all appear to cross over around $P_g^\star \sim 1$ kPa, the experimental results do so at higher values of $P_g^\star$, with the two highest-viscosity solutions crossing over at $P_g^\star \sim 10$ kPa.

In summary, while all of the qualitative features of the experimental results are recovered in our computations, quantitative agreement is not good over the entire range of data. In particular, less pressure reduction is required in the experiments than in the computations for there to be a noticeable effect on the maximum wetting speed. There are a number of possible reasons for this discrepancy, some of which we will now consider.

Roughness of the solid: In Benkreira & Khan (2008) the 'average peak-to-valley height roughness' for the experimental results presented is 300 nm. Although this is

https://doi.org/10.1017/jfm.2015.121 Published online by Cambridge University Press

'smooth' compared with the other solids used in this work, it is still quite rough compared with the solids used in some other coating flow studies. This effect cannot be ignored as experiments in Clarke (2002) have demonstrated that the roughness of a solid can influence the maximum speed of wetting with, in many cases, faster coating speeds obtained with rougher surfaces.

From a modelling perspective, the level of roughness in the experiments is large when compared with the slip length at the liquid–solid interface $l_s^\star = 10$ nm. However, simply increasing the value of $l_s^\star$ in an attempt to mimic the effect of the roughness does not capture the experimental data either. It is likely that the strongest effect of the roughness will be on the actual contact angle, but a theoretical description of this mechanism at high contact-line speeds remains an open problem and is beyond the scope of this work.

Dynamics of the contact angle: Despite assuming that the contact angle is fixed at its equilibrium value, without fitting the slip length in any way we still obtain reasonable agreement for the values of $U_c^\star$ at atmospheric pressure. This could be a coincidence and dynamic contact angle effects may indeed be important for quantitatively capturing this class of coating flows; however, such effects will not improve the agreement of our present model with experiments. This is because allowing the contact angle to vary will increase the angle from its equilibrium value so that, as shown by the findings of § 5.3, $U_c^\star$ will decrease for a given pressure. Therefore, although the dynamics of the contact angle will alter our results, it will not explain why Ca_c increases so quickly with reductions in $\bar{P}_g$ and is thus not our main concern here.

Model for non-equilibrium effects: As shown in § 4.3, the Knudsen number characterising the gas film flow indicated that its dynamics is usually outside the 'slip regime' as air entrainment is approached and more complex non-equilibrium gas dynamics should be incorporated. As noted in § 4.3, incorporation of these effects is likely to result in the same qualitative trends but enhanced quantitative ones. In particular, it is likely that less gas will be driven into the contact-line region at a given pressure so that there is an enhancement in Ca_c at higher ambient pressures, as observed experimentally. Furthermore, this effect will be particularly important at smaller $\bar{\mu}$, where most of the current discrepancies between theory and experiment appear, as the smaller values of H obtained there (Vandre *et al.* 2013) will increase the importance of non-equilibrium effects. Models capable of predicting these effects will be discussed in § 8.

The most likely cause of the observed discrepancy seems to be our inadequate description of the gas dynamics, and this aspect will be discussed further in § 8. Before doing so, we consider what consequences our results have for the drop impact phenomenon.

7. Non-equilibrium gas effects in drop impact phenomena

It has previously been suggested (Rein & Delplanque 2008), that certain classes of splash observed in drop impact phenomena are triggered by the same mechanisms that cause wetting failure in coating flows. This interpretation is supported by experiments such as those in Driscoll & Nagel (2011), who find 'No trapped air beneath the spreading drop outside the small central bubble; there is no significant air film beneath the drop at the time of thin-sheet ejection. This suggests that, rather than an underlying air layer, gas flow at the edge of the spreading drop is responsible for destabilising the liquid.' This mechanism is shown by figure 1(*b*). Therefore, we now

https://doi.org/10.1017/jfm.2015.121 Published online by Cambridge University Press

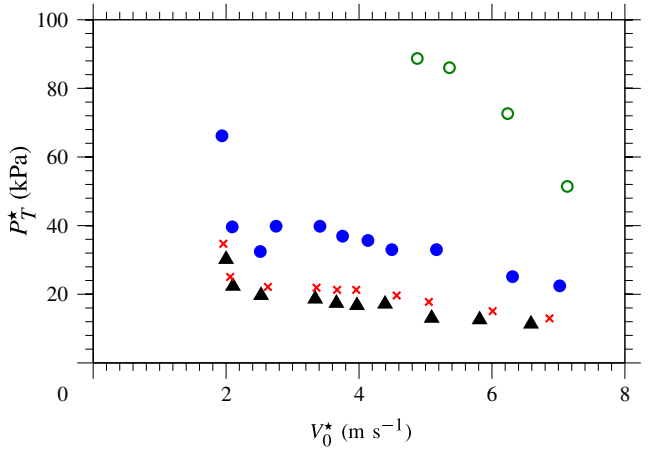

FIGURE 17. (Colour online) Critical gas pressure $P_T^\star$ required to suppress the splash of a drop with impact speed $V_0^\star$ with different gases: helium (open circles in green), air (filled circles in blue), krypton (red crosses) and SF_6 (triangles in black). Obtained from Xu *et al.* (2005).

consider how our results can be related to the more complex unsteady drop impact phenomenon.

The publication that opened up this field of research was Xu *et al.* (2005). This work focuses on a threshold ambient pressure $P_T^\star$ that must be achieved in order to suppress splashing for a particular liquid–solid–gas configuration. What is particularly interesting is that for a given impact speed $V_0^\star$, the threshold pressure strongly depends on the gas, with air, helium, krypton and SF_6 all used. The data are shown in figure 17, which corresponds in Xu *et al.* (2005) to the inset of their figure 2(*b*). In Xu *et al.* (2005), compressibility effects in the gas are assumed to be important when deriving a splash threshold, so that changes in the molecular mass of the gases $m_g^\star$, which alter the speed of sound in the gas, become important and result in a collapse of the data when $P_T^\star$ is scaled by $\sqrt{m_g^\star/m_{air}^\star}$, where $m_{air}^\star$ is the molecular mass of air.

An alternative explanation is that compressibility effects are negligible and that increased Maxwell slip is responsible for splash suppression at reduced pressure. Given that the mean free path in the gas at the threshold point $\ell_T^\star$ is inversely proportional to both the gas pressure and the square root of the molecular mass $\ell_T^\star \propto (P_T^\star\sqrt{m_g^\star})^{-1}$, to achieve a given $\ell_T^\star$, increases in $m_g^\star$ require decreases in $P_T^\star$. In other words, gases with higher molecular mass will need lower pressures to suppress splashing, as seen in Xu *et al.* (2005).

The dimensionless number characterising the level of Maxwell slip at a given threshold pressure in the gas is the Knudsen number $Kn_T = \ell_T^\star/R^\star$, where $R^\star = 1.7$ mm is the drop radius. Using the properties of air, the expression for Kn_T required is

$$Kn_T = \frac{Kn_{air,atm}}{\sqrt{\tilde{m}_g}\bar{P}_T}, \quad \text{where } \bar{P}_T = \frac{P_T^\star}{P_{atm}^\star} \text{ and } \tilde{m}_g = \frac{m_g^\star}{m_{air}^\star}, \tag{7.1}$$

where the coefficient of proportionality $Kn_{air,atm} = 4.1 \times 10^{-5}$ is the Knudsen number of air at atmospheric pressure and the molecular weights in daltons of $m_{He}^\star = 4$,

https://doi.org/10.1017/jfm.2015.121 Published online by Cambridge University Press

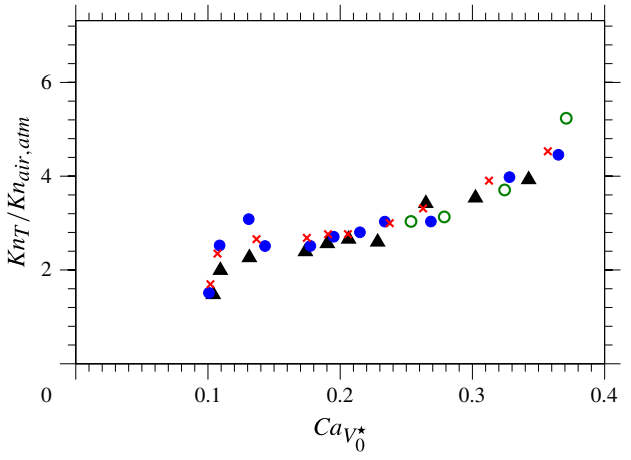

FIGURE 18. (Colour online) Critical Knudsen number Kn_T, scaled by its value in air at atmospheric pressure, required to suppress the splash of a drop whose capillary-number-based impact speed is $Ca_{V_0^\star}$. The collapse of data from figure 17 onto a single curve is apparent.

$m^\star_{air} = 29$, $m^\star_{\mathrm{Kr}} = 83.8$ and $m^\star_{\mathrm{SF}_6} = 146$ can be taken from Xu *et al.* (2005). As for the coating flow analysis, the value of the Knudsen number has to be based on the global characteristics of the flow and would be larger if it could have been derived from the appropriate length scales near the moving contact line.

Ideally, the collapse of data would use Kn_T and a capillary number based on the contact-line speed $U^\star$ at the point of air entrainment, as considered for the coating flow analysis. However, such measurements were not made in the experimental work so we shall instead base the capillary number $Ca_{V_0^\star}$ on the impact speed $V_0^\star$, an assumption that will be discussed in § 8.

In figure 18, the raw data from figure 17 are shown to collapse well onto axes of $Ca_{V_0^\star}$ versus Kn_T. This is encouraging, and suggests that non-equilibrium effects in the gas may be important for drop impact phenomena. It is particularly reassuring to see that the capillary numbers obtained are within the range one may expect for air entrainment phenomena to be occurring, although the capillary number based on the contact-line speed at the entrainment point may be much larger. Ideally, changes in the viscosity of the liquid would also be included into the data collapse, as achieved in Xu *et al.* (2005), but this is not possible here as such variations cannot simply be absorbed into the capillary number, but will also alter many other dominant parameters such as the viscosity ratio.

Although the data collapse looks impressive, a number of outstanding questions remain. First, as also seen in § 6, experimentally only relatively small changes in atmospheric pressure are required to suppress splashing, with a factor of 10 decrease sufficient to prevent it in all cases considered here (figure 17), and it remains to be seen whether the Maxwell-slip model is able to predict such a large effect at these reduced pressures. Second, in this framework it is not obvious why the drop spreads for some distance before splashing, when the largest contact-line speeds are obtained earliest in the impact process. These two issues will be addressed in § 8 and will require further experimental and theoretical work before they can be fully resolved.

https://doi.org/10.1017/jfm.2015.121 Published online by Cambridge University Press

8. Discussion

It has been shown that non-equilibrium effects in a gas, influencing the flow through Maxwell slip at boundaries, can substantially increase the critical speed at which air entrainment occurs. Notably, neglecting to use slip at the gas–liquid boundary produces qualitatively different results from those obtained when slip is allowed, predicting a finite, rather than unbounded, maximum speed of wetting as the pressure is reduced. Importantly, the problem has been formulated locally, so that the model is valid for any shape of the gas domain and remains accurate both far away from the gas film, where non-equilibrium gas effects will have a negligible influence on the overall flow, as well as very close to the contact line, where regions of high curvature invalidate the lubrication approximation.

The model proposed was shown to reproduce many of the features of the experimental results in Benkreira & Khan (2008) but failed to accurately predict the ambient pressures at which coating speeds begin to rise for the higher-viscosity liquids. These observations open up a number of potential areas for experimental and theoretical research which will now be considered.

8.1. *Extension of the non-equilibrium gas model*

General research into non-equilibrium gas dynamics has identified different 'regimes' of flow which indicate the modelling approach that should be used. Application of these to the flow in the gas film, characterised by Kn_H, gives the following.

Conventional regime ($Kn_H < 10^{-3}$): The Navier–Stokes equations with no-slip at solid surfaces provide an accurate representation of the gas flow.

Slip regime ($10^{-3} < Kn_H < 10^{-1}$): Non-equilibrium effects become significant close to the boundary so that the no-slip condition must be relaxed to allow for Maxwell slip.

Transition regime ($10^{-1} < Kn_H < 10$): Knudsen layers occupy significant proportions of the domain and kinetic theory is required to provide reliable predictions.

Free molecular flow regime ($Kn_H > 10$): Molecular collisions become rare so that the collision operator in the Boltzmann equation can be neglected.

Clearly, identification of which regime is important for the dynamic wetting problems of interest will be key to deciding which methods should be implemented.

The Knudsen numbers recovered for the gas film flow show that in many cases the model proposed in § 2 has been used outside its limits of applicability. In particular, once in the transition regime the effect of Knudsen layers can no longer be accurately captured by a first-order slip condition, as assumed here. An entire hierarchy of approaches of varying complexity have been proposed in the published literature to overcome this inadequacy, and which of these is optimum for the class of problem considered here is, at present, unclear. A sensible first step would be to remain within a continuum framework and to incorporate more advanced non-equilibrium gas effects either, in the simplest case, by using a second-order slip condition, such as that proposed in Hadjiconstantinou (2003), or, at the next level of difficulty, by modifying the bulk constitutive relations also (Lockerby, Reese & Gallis 2005*a*). Research in this direction is currently underway.

The regions of applicability of the aforementioned approaches are often unclear, and the only way to test these is to compare with solutions obtained from the Boltzmann equation. This can now be routinely achieved using a variety of methods, with the direct simulation Monte Carlo (DSMC) approach being popular (Bird 1994).

https://doi.org/10.1017/jfm.2015.121 Published online by Cambridge University Press

However, in this setting it is not clear how the liquid–gas free surface should be treated as the Boltzmann equation cannot be applied across the boundary and into the liquid phase. Whether some plausible assumptions about the liquid free-surface properties could be made or whether DSMC in the gas could somehow be coupled to molecular dynamics simulations (Koplik & Banavar 1995) in the bulk of the liquid remains to be seen. Progress in the latter area would shed light on not only the bulk flow of the gas, but also its interaction with boundaries formed by liquids.

8.2. *Alternative flow configurations*

It is of interest to look at the effects of gas pressure on coating speeds in a range of different set-ups, both experimentally and theoretically. In particular, the effects of confinement, where the contact line is isolated by a nearby boundary, have not been considered, and neither have axisymmetric geometries such as those used in fibre coating.

The fibre coating configuration is particularly interesting as experiments in Simpkins & Kuck (2003) show that extremely high capillary numbers can be achieved before air entrainment occurs and, at present, the precise cause for this remains to be seen. Some works claim that the same mechanism has been observed in hydrodynamic assist (Blake, Dobson & Ruschak 2004), while others have proposed that air is actually entrained into the liquid but then dissolved due to the high pressures there (Jacqmin 2002). Incorporation of the models proposed into the computational framework developed here should allow one to distinguish between these rival interpretations.

8.3. *Development of analytic theory*

The theory of Cox (1986) has been used widely to calculate an apparent contact angle from its actual value in both single- and two-phase dynamic wetting phenomena. Although this theory is based on a small-capillary-number asymptotics, so that it lacks accuracy for many coating flows (Vandre *et al.* 2013), it nevertheless has been a useful tool for interpreting experiments and predicts a possible mechanism by which air entrainment can occur; namely, that once the apparent angle reaches 180°, no more solutions can be obtained. However, in its present state this theory cannot capture the phenomena investigated in this paper.

Cox's theory contains an 'inner region' where additional effects come into play, such as slip, which allow the moving contact-line problem to be circumvented. When one has the same slip length in each phase, then the theory is valid, but for the problems we have considered the slip in the gas phase is many times larger than that in the liquid. In particular, the slip length in the gas phase is likely to become comparable with the scale of the 'intermediate region', where the bending of the free surface occurs, so that the entire asymptotic structure of the problem becomes unclear. It would be of interest to see whether Cox's approach can be generalised for this more complex class of flows.

8.4. *Parametric experimental study of dip coating at reduced pressures*

The results of Benkreira & Khan (2008) have allowed us to compare our computational results with experimental data. However, these are, at present, the only results in the published literature considering the effect of gas pressure on coating processes. Therefore, additional experimental studies would be useful in order to develop the theory of this class of problems. Such an investigation could, for example, use a wider variety of liquids and consider solids with a range of different wettabilities

https://doi.org/10.1017/jfm.2015.121 Published online by Cambridge University Press

and/or roughnesses. Furthermore, consideration of how accelerating or decelerating the plate alters the flow may give some initial insight into more complex unsteady flows such as drop impact.

If the aforementioned analyses could be combined with modern experimental techniques, such as interferometry measurements, then some details of the gas film profile could potentially be recovered, as has been achieved in drop impact phenomena. These results would provide an excellent benchmark for any potential theories to be compared with.

8.5. *Drop impact and spreading*

Drop impact phenomena are notoriously difficult to capture computationally due to the inherently multiscale nature of a problem that involves unsteady large deformation of the flow domain. Although this has been achieved in the case of a single-phase flow, e.g. in Sprittles & Shikhmurzaev (2012*b*), at present there are no codes that have captured all physical scales in (*a*) the dynamics of impact, where a thin gas film cushions the falling drop, (*b*) the topological change, when the drop first touches the solid, and (*c*) the spreading process, where the slip length needs to be resolved. The construction of a code capable of achieving this goal is highly sought after.

A question arising from our analysis in § 7 is why the drop spreads for some distance before splashing, when its highest speeds are obtained early on in the impact process. The answer to this question is likely to involve the shape of the drop and its flow field, so that one cannot simply consider an isolated moving contact line, as we have done, but must also consider the outer influence of the flow field on the point at which air entrainment occurs.

The situation with drop impact could be similar to that of curtain coating, where the point at which air entrainment occurs is dependent not only on the contact-line speed, but also on the flow geometry (Blake, Clarke & Ruschak 1994; Clarke & Stattersfield 2006). In particular, when the contact line is below the falling liquid curtain it appears to be 'assisted' by the downward pressure of the curtain (Blake *et al.* 2004), which prevents air entrainment, while if a heel forms in the free surface the contact line becomes isolated from the bulk flow and there is no assist. Similarly, in drop impact, during the initial stages of spreading the contact line is located below the drop, and thus wetting is assisted by the downward pressure of the bulk flow, until a lamella is ejected, analogous to a heel in curtain coating. At this point, the contact line is isolated and air entrainment between the lamella and the substrate is able to lift off a sheet of liquid which creates a splash.

In order to determine whether the aforementioned mechanism is the correct one for drop impact phenomena, it may still be useful to use the simpler coating flow set-ups. One possibility is that the influence of an impulsively started or accelerating plate could be considered in such a manner as to mimic the impact process. Another avenue of enquiry would be to alter the flow domain to mimic the flux of mass arriving at the contact line in drop impact phenomena.

From an experimental perspective, it would be extremely useful to know the contact-line speed at the point of air entrainment, so that the capillary numbers used in § 7 could be based on this, rather than the impact speed. In particular, if air entrainment occurs after the drop contact line has moved a radius $r_s^\star$, and the contact line moves with a square root in time dependence, as shown experimentally (Riboux & Gordillo 2014) for the initial stages of motion, so that $r_s^\star/R^\star = A\sqrt{V_0^\star t^\star/R^\star}$ and $U^\star/V_0^\star = A/2\sqrt{R^\star/(V_0^\star t^\star)}$, where A is a constant, we find that $U^\star/V_0^\star = (A^2/2)R^\star/r_s^\star$. Therefore, $Ca_{V_0^\star}$ is only a fixed multiple of Ca if air entrainment always occurs at

https://doi.org/10.1017/jfm.2015.121 Published online by Cambridge University Press

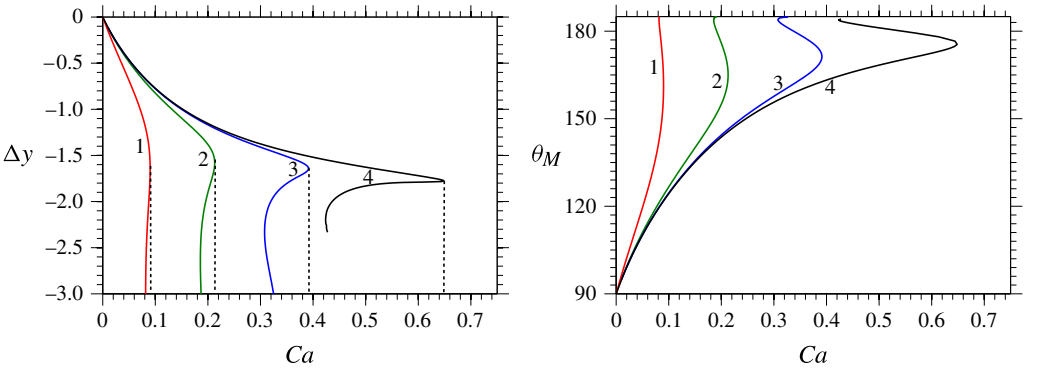

FIGURE 19. (Colour online) Dependence of the elevation Δy and maximum apparent contact angle θ_M on the capillary number Ca for $\bar{\mu} = 1, 10^{-1}; 2, 10^{-2}; 3, 10^{-3}; 4, 10^{-4}$ and other parameters listed in the text. The dashed lines indicate the critical capillary number $Ca = Ca_c$ past which no steady-state solutions exist.

the same radius $r_s^\star$, which seems unlikely to be the case across all parameter space. Therefore, we cannot be sure that $Ca_c \propto Ca_{V_0^\star}$ and more experimental data are indeed required.

Acknowledgements

The author would like to thank T. Blake and Y. Shikhmurzaev for numerous insightful discussions and continual encouragement over the years, D. Lockerby for lending his expertise with aspects of the gas dynamics, E. Vandre for stimulating conversations about coating flows, and the referees of the paper whose valuable comments helped to improve the manuscript.

Appendix A. Benchmark calculations

From a theoretical perspective, both extended lubrication theory (Chan *et al.* 2013) and full computations (Vandre *et al.* 2012, 2013) have identified a critical capillary number past which no steady two-dimensional solutions exist, and it has been assumed that this corresponds to the Ca_c observed in experiments. As initially observed for the plate withdrawal problem, i.e. the dewetting scenario (Snoeijer *et al.* 2007), the turning point at Ca_c in the map of elevation Δy (or maximum apparent contact angle θ_M) versus Ca separates stable and unstable branches of steady-state solutions (figure 19). Consequently, when considering the entire solution space, for certain Ca multiple values of elevation Δy exist, and no function $\Delta y = \Delta y(Ca)$ exists. Notably though, along all sections of the solution path we have $Ca < Ca_c$, so that Ca_c is indeed the maximum speed of wetting.

In order to determine Ca_c for a given system, a number of possible solution techniques exist. The most obvious approach is to find a solution at a relatively small Ca, then increase its value, using the previous computed solution as an initial guess for the next Ca, and repeat until no more steady-state solutions exist. This is the simplest method and reliably finds Ca_c, but it does not allow us to extract the solution path past the critical point where $Ca < Ca_c$, as noted in Vandre *et al.* (2012). A different approach, which allows the entire solution path to be captured, is to determine Ca, i.e. treat it as an unknown in the problem, for a fixed elevation of the contact line Δy. This approach works better in practice, as for every Δy, there

https://doi.org/10.1017/jfm.2015.121 Published online by Cambridge University Press

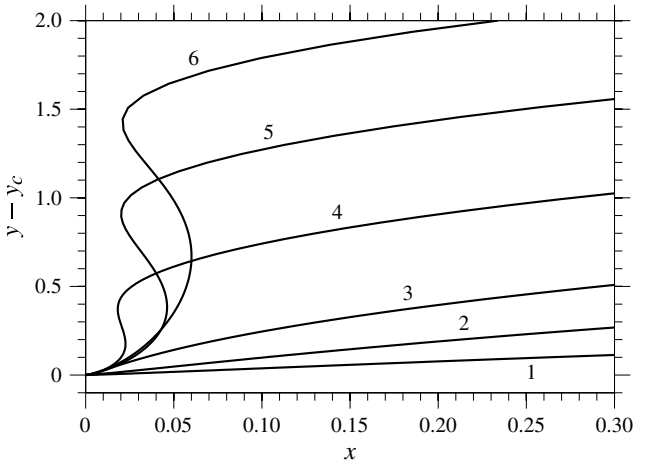

FIGURE 20. Free-surface profiles for the case of $\bar{\mu} = 10^{-3}$ at different elevations: 1, $\Delta y = -0.5$; 2, $\Delta y = -1$; 3, $\Delta y = -1.5$; 4, $\Delta y = -2$; 5, $\Delta y = -2.5$; 6, $\Delta y = -3$.

is a unique Ca, i.e. there is a function $Ca = Ca(\Delta y)$. Consequently, curves like those in figure 19 can be generated.

In principle, as much of the unstable branch as required can be captured, but for $\Delta y \ll \Delta y_{crit}$, where Δy_{crit} is the elevation when $Ca = Ca_c$, the deformation of the free surface becomes large and this process becomes computationally intensive, particularly at small $\bar{\mu}$. Consequently, simulations were run up to the point in the solution path where the mesh failed, usually due to the finite elements becoming too distorted, and stopped there. As one can see from figure 19, all simulations were extended well past $\Delta y = \Delta y_{crit}$, and it was only the smallest viscosity ratio (curve 4) where the code finished prematurely, i.e. before $\Delta y = -3$.

A.1. *Calculations and comparison with Vandre et al. (2013)*

In order to compare our computations with previous work in Vandre *et al.* (2013), consider Stokes flow $Oh^{-1} = 0$, with the slip lengths of the liquid–solid and gas–solid interfaces equal at $l_s = Kn = 10^{-4}$, no-slip across the liquid–gas interface, so that $A = 0$, and a constant contact angle of $\theta_d = 90°$. Using these parameters, the critical capillary number Ca_c and maximum apparent contact angle at this point θ_M, which occurs at the inflection point on the free surface (see figure 2), are computed for different viscosity ratios $\bar{\mu} = 10^{-1}$, 10^{-2}, 10^{-3}, 10^{-4} and compared with the results in Vandre *et al.* (2013).

In figure 19, the dependences of Δy and θ_M on Ca are computed. From the curves one can clearly see the existence of a critical capillary number Ca_c past which ($Ca > Ca_c$) no solutions exist. On further decreasing Δy, so that the contact line moves further down the plate, solutions are recovered for which $Ca < Ca_c$, and the capillary number begins to oscillate around a capillary number $Ca^* < Ca_c$ as also observed in theoretical works on dewetting phenomena, where these solutions have been shown to correspond to a series of saddle–node bifurcations, see figures 4 and 5 of Snoeijer *et al.* (2007), which are related to transient states (Snoeijer *et al.* 2006).

Similar oscillations are observed for θ_M, where, notably, along the unstable branch the maximum apparent angle can increase beyond 180°. This can be seen in figure 20, where between curves 3 and 4 a hump develops in the free-surface profile. In this

https://doi.org/10.1017/jfm.2015.121 Published online by Cambridge University Press

$\bar{\mu}$	Ca_c		$\theta_M(Ca_c)$	
	Computed	Vandre *et al.* (2013)	Computed (deg.)	Vandre *et al.* (2013) (deg.)
10^{-1}	0.09	0.09	161	159
10^{-2}	0.21	0.22	165	166
10^{-3}	0.39	0.41	171	172
10^{-4}	0.65	0.65	176	176

TABLE 2. Comparison of the critical capillary number Ca_c and free-surface angle at the inflection point θ_M obtained from our code with those obtained in Vandre *et al.* (2013) across a range of viscosity ratios $\bar{\mu}$.

region, the gradient of the free surface is negative so that the angle that this portion makes with the solid, i.e. the apparent angle, gives a maximum of $\theta_M > 180°$.

A comparison between the critical capillary numbers computed in Vandre *et al.* (2013) and those observed here is not likely to be exact, as different flow geometries have been used. However, in cases where Ca_c is not too large and the effect of the flow geometry is relatively weak we may expect our values to be comparable with theirs. In table 2 this is shown to be the case. The computed values of both Ca_c and θ_M at this capillary number, which is a very sensitive measure, agree well across a large range of viscosity ratios. It is not our intention to analyse these data in detail, as this has already been achieved in Vandre *et al.* (2013), but this table will be useful as a benchmark for future computational work in this area.

REFERENCES

AGARWAL, A. & PRABHU, S. V. 2008 Survey on measurement of tangential momentum accommodation coefficient. *J. Vac. Sci. Technol.* A **26**, 634–645.

ALLEN, M. D. & RAABE, O. G. 1982 Re-evaluation of Millikan's oil drop data for the motion of small particles in air. *J. Aerosol Sci.* **6**, 537–547.

ANDREWS, M. K. & HARRIS, P. D. 1995 Damping and gas viscosity measurements using a microstructure. *Sensors Actuators* A **49**, 103–108.

BENKREIRA, H. & IKIN, J. B. 2010 Dynamic wetting and gas viscosity effects. *Chem. Engng Sci.* **65**, 1790–1796.

BENKREIRA, H. & KHAN, M. I. 2008 Air entrainment in dip coating under reduced air pressures. *Chem. Engng Sci.* **63**, 448–459.

BIRD, G. A. 1994 *Molecular Gas Dynamics and the Direct Simulation of Gas Flows*. Clarendon.

BLAKE, T. D. 2006 The physics of moving wetting lines. *J. Colloid Interface Sci.* **299**, 1–13.

BLAKE, T. D., CLARKE, A. & RUSCHAK, K. J. 1994 Hydrodynamic assist of wetting. *AIChE J.* **40**, 229–242.

BLAKE, T. D. & DE CONINCK, J. 2002 The influence of solid–liquid interactions on dynamic wetting. *Adv. Colloid Interface Sci.* **96**, 21–36.

BLAKE, T. D., DOBSON, R. A. & RUSCHAK, K. J. 2004 Wetting at high capillary numbers. *J. Colloid Interface Sci.* **279**, 198–205.

BLAKE, T. D. & HAYNES, J. M. 1969 Kinetics of liquid/liquid displacement. *J. Colloid Interface Sci.* **30**, 421–423.

BLAKE, T. D. & RUSCHAK, K. J. 1979 A maximum speed of wetting. *Nature* **282**, 489–491.

BLAKE, T. D. & SHIKHMURZAEV, Y. D. 2002 Dynamic wetting by liquids of different viscosity. *J. Colloid Interface Sci.* **253**, 196–202.

BOUWHUIS, W., VAN DER VEEN, R. C. A., TRAN, T., KEIJ, D. L., WINKELS, K. G., PETERS, I. R., VAN DER MEER, D., SUN, C., SNOEIJER, J. H. & LOHSE, D. 2012 Maximal air bubble entrainment at liquid-drop impact. *Phys. Rev. Lett.* **109**, 264501.

https://doi.org/10.1017/jfm.2015.121 Published online by Cambridge University Press

BURLEY, R. & KENNEDY, B. S. 1976 An experimental study of air entrainment at a solid/liquid/gas interface. *Chem. Engng Sci.* **31**, 901–911.

BUSSMANN, M., CHANDRA, S. & MOSTAGHIMI, J. 2000 Modeling the splash of a droplet impacting a solid surface. *Phys. Fluids* **12**, 3121–3132.

CERCIGNANI, C. 2000 *Rarefied Gas Dynamics: From Basic Concepts to Actual Calculations*. Cambridge University Press.

CHAN, T. S., SRIVASTAVA, S., MARCHAND, A., ANDREOTTI, B., BIFERALE, L., TOSCHI, F. & SNOEIJER, J. H. 2013 Hydrodynamics of air entrainment by moving contact lines. *Phys. Fluids* **25**, 074105.

CHAPMAN, S. & COWLING, T. G. 1970 *The Mathematical Theory of Non-Uniform Gases: An Account of the Kinetic Theory of Viscosity, Thermal conduction and Diffusion in Gases*. Cambridge University Press.

CLARKE, A. 2002 Coating on a rough surface. *AIChE J.* **48**, 2149–2156.

CLARKE, A. & STATTERSFIELD, E. 2006 Direct evidence supporting nonlocal hydrodynamic influence on the dynamic contact angle. *Phys. Fluids* **18**, 048106.

COX, R. G. 1986 The dynamics of the spreading of liquids on a solid surface. Part 1. Viscous flow. *J. Colloid Interface Sci.* **168**, 169–194.

DE CONINCK, J. & BLAKE, T. D. 2008 Wetting and molecular dynamics simulations of simple fluids. *Annu. Rev. Mater. Res.* **38**, 1–22.

DEJAGUIN, B. V. & LEVI, S. M. 1964 *Film Coating Theory*. Focal.

DERBY, B. 2010 Inkjet printing of functional and structural materials: fluid property requirements, feature stability and resolution. *Annu. Rev. Mater. Res.* **40**, 395–414.

DRISCOLL, M. M. & NAGEL, S. R. 2011 Ultrafast interference imaging of air in splashing dynamics. *Phys. Rev. Lett.* **107**, 154502.

DUCHEMIN, L. & JOSSERAND, C. 2012 Rarefied gas correction for the bubble entrapment singularity in drop impacts. *C. R. Méc.* **340**, 797–803.

DUEZ, C., YBERT, C., CLANET, C. & BOCQUET, L. 2007 Making a splash with water repellency. *Nat. Phys.* **3**, 180–183.

DUSSAN, E. B. V. 1976 The moving contact line: the slip boundary condition. *J. Fluid Mech.* **77**, 665–684.

DUSSAN, E. B. V. 1977 Immiscible liquid displacement in a capillary tube: the moving contact line. *AIChE J.* **23**, 131–133.

DUSSAN, E. B. V. & DAVIS, S. H. 1974 On the motion of a fluid–fluid interface along a solid surface. *J. Fluid Mech.* **65**, 71–95.

DUSSAN, E. B. V., RAMÉ, E. & GAROFF, S. 1991 On identifying the appropriate boundary conditions at a moving contact line: an experimental investigation. *J. Fluid Mech.* **230**, 97–116.

EGGERS, J. 2004 Hydrodynamic theory of forced dewetting. *Phys. Rev. Lett.* **93**, 094502.

EGGERS, J., FONTELOS, M. A., JOSSERAND, C. & ZALESKI, S. 2010 Drop dynamics after impact on a solid wall: theory and simulations. *Phys. Fluids* **22**, 062101.

GAD-EL-HAK, M. (Ed.) 2006 Flow physics. In *MEMS: Introduction and Fundamentals*, 4-1–36, CRC.

HADJICONSTANTINOU, N. G. 2003 Comment on Cercignani's second-order slip coefficient. *Phys. Fluids* **15**, 2352–2354.

HOCKING, L. M. 1976 A moving fluid interface on a rough surface. *J. Fluid Mech.* **76**, 801–807.

HOFFMAN, R. L. 1975 A study of the advancing interface. I. Interface shape in liquid–gas systems. *J. Colloid Interface Sci.* **50**, 228–241.

HUH, C. & MASON, S. G. 1977 The steady movement of a liquid meniscus in a capillary tube. *J. Fluid Mech.* **81**, 401–409.

HUH, C. & SCRIVEN, L. E. 1971 Hydrodynamic model of steady movement of a solid/liquid/fluid contact line. *J. Colloid Interface Sci.* **35**, 85–101.

JACQMIN, D. 2002 Very, very fast wetting. *J. Fluid Mech.* **455**, 347–358.

KISTLER, S. F. 1993 Hydrodynamics of wetting. In *Wettability* (ed. J. C. Berg), pp. 311–429. Marcel Dekker.

https://doi.org/10.1017/jfm.2015.121 Published online by Cambridge University Press

KISTLER, S. F. & SCRIVEN, L. E. 1983 Coating flows. In *Computational Analysis of Polymer Processing* (ed. J. R. A. Pearson & S. M. Richardson), pp. 243–299. Applied Science Publishers.

KOLINSKI, J. M., MAHADEVAN, L. & RUBINSTEIN, S. M. 2014 Drops can bounce from perfectly hydrophilic surfaces. *Europhys. Lett.* **108**, 24001.

KOLINSKI, J. M., RUBINSTEIN, S. M., MANDRE, S., BRENNER, M. P., WEITZ, D. A. & MAHADEVAN, L. 2012 Skating on a film of air: drops impacting on a surface. *Phys. Rev. Lett.* **108**, 074503.

KOPLIK, J. & BANAVAR, J. R. 1995 Continuum deductions from molecular hydrodynamics. *Annu. Rev. Fluid Mech.* **27**, 257–292.

LAUGA, E., BRENNER, M. & STONE, H. A. 2007 Microfluidics: the no-slip boundary condition. In *Springer Handbook of Experimental Fluid Mechanics*, pp. 1219–1240. Springer.

LIU, Y., TAN, P. & XU, L. 2015 Kelvin–Helmholtz instability in an ultrathin air film causes drop splashing on smooth surfaces. *Proceedings of the National Academy of Sciences*.

LOCKERBY, D. A., REESE, J. M., EMERSON, D. R. & BARBER, R. W. 2004 Velocity boundary condition at solid walls in rarefied gas calculations. *Phys. Rev.* E **70**, 017303.

LOCKERBY, D. A., REESE, J. M. & GALLIS, M. A. 2005*a* Capturing the Knudsen layer in continuum-fluid models of nonequilibrium gas flows. *AIAA J.* **43**, 1391–1393.

LOCKERBY, D. A., REESE, J. M. & GALLIS, M. A. 2005*b* The usefulness of higher-order constitutive relations for describing the Knudsen layer. *Phys. Fluids* **17**, 100609.

MANDRE, S. & BRENNER, M. P. 2012 The mechanism of a splash on a dry solid surface. *J. Fluid Mech.* **690**, 148–172.

MANI, M., MANDRE, S. & BRENNER, M. P. 2010 Events before droplet splashing on a solid surface. *J. Fluid Mech.* **647**, 163–185.

MARCHAND, A., CHAN, T. S., SNOEIJER, J. H. & ANDREOTTI, B. 2012 Air entrainment by contact lines of a solid plate plunged into a viscous fluid. *Phys. Rev. Lett.* **108**, 204501.

MAXWELL, J. C. 1867 On the dynamical theory of gases. *Phil. Trans. R. Soc. Lond.* **157**, 49–88.

MAXWELL, J. C. 1879 On stresses in rarified gases arising from inequalities of temperature. *Phil. Trans. R. Soc. Lond.* **170**, 231–256.

MILLIKAN, R. A. 1923 The general law of fall of a small spherical body through a gas, and its bearing upon the nature of molecular reflection from surfaces. *Phys. Rev.* **22**, 1–23.

MUES, W., HENS, J. & BOIY, L. 1989 Observation of a dynamic wetting process using laser-Doppler velocimetry. *AIChE J.* **35**, 1521–1526.

NAVIER, C. L. M. H. 1823 Mémoire sur les lois mouvement des fluides. *Mém. Présentés par Divers Savants Acad. Sci. Inst. Fr.* **6**, 389–440.

NGAN, C. G. & DUSSAN, E. B. V. 1982 On the nature of the dynamic contact angle: an experimental study. *J. Fluid Mech.* **118**, 27–40.

RAMÉ, E. & GAROFF, S. 1996 Microscopic and macroscopic dynamic interface shapes and the interpretation of dynamic contact angles. *J. Colloid Interface Sci.* **177**, 234–244.

REIN, M. 1993 Phenomena of liquid drop impact on solid and liquid surfaces. *Fluid Dyn. Res.* **12**, 61–93.

REIN, M. & DELPLANQUE, J.-P. 2008 The role of air entrainment on the outcome of drop impact on a solid surface. *Acta Mechanica* **201**, 105–118.

RIBOUX, G. & GORDILLO, J. M. 2014 Experiments of drops impacting a smooth solid surface: a model of the critical impact speed for drop splashing. *Phys. Rev. Lett.* **113**, 024507.

DE RUITER, J., LAGRAAUW, R., ENDE, D. & MUGELE, F. 2015 Wettability-independent bouncing on flat surfaces mediated by thin air films. *Nat. Phys.* **11**, 48–53.

DE RUITER, J., OH, J. M., ENDE, D. & MUGELE, F. 2012 Dynamics of collapse of air films in drop impact. *Phys. Rev. Lett.* **108**, 074505.

RUSCHAK, K. J. 1980 A method for incorporating free boundaries with surface tension in finite element fluid-flow simulators. *Intl J. Numer. Meth. Engng* **15**, 639–648.

SCHROLL, R. D., JOSSERAND, C., ZALESKI, S. & ZHANG, W. W. 2010 Impact of a viscous liquid drop. *Phys. Rev. Lett.* **104**, 034504.

https://doi.org/10.1017/jfm.2015.121 Published online by Cambridge University Press

SHIKHMURZAEV, Y. D. 1997 Moving contact lines in liquid/liquid/solid systems. *J. Fluid Mech.* **334**, 211–249.

SHIKHMURZAEV, Y. D. 2006 Singularities at the moving contact line. Mathematical, physical and computational aspects. *Physica* D **217**, 121–133.

SHIKHMURZAEV, Y. D. 2007 *Capillary Flows with Forming Interfaces*. Chapman & Hall/CRC.

SIMMONS, J. A., SPRITTLES, J. E. & SHIKHMURZAEV, Y. D. 2015 The formation of a bubble from a submerged orifice. *Eur. J. Mech. (*B*/Fluids)*. (in press).

SIMPKINS, P. G. & KUCK, V. J. 2003 On air entrainment in coatings. *J. Colloid Interface Sci.* **263**, 562–571.

SMITH, F. T., LI, L. & WU, G. X. 2003 Air cushioning with a lubrication/inviscid balance. *J. Fluid Mech.* **482**, 291–318.

SNOEIJER, J. H. & ANDREOTTI, B. 2013 Moving contact lines: scales, regimes, and dynamical transitions. *Annu. Rev. Fluid Mech.* **45**, 269–292.

SNOEIJER, J. H., ANDREOTTI, B., DELON, G. & FERMIGIER, M. 2007 Relaxation of a dewetting contact line. Part 1. A full-scale hydrodynamic calculation. *J. Fluid Mech.* **579**, 63–83.

SNOEIJER, J. H., DELON, G., FERMIGIER, M. & ANDREOTTI, B. 2006 Avoided critical behavior in dynamically forced wetting. *Phys. Rev. Lett.* **96**, 174504.

SPRITTLES, J. E. & SHIKHMURZAEV, Y. D. 2012*a* Coalescence of liquid drops: different models versus experiment. *Phys. Fluids* **24**, 122105.

SPRITTLES, J. E. & SHIKHMURZAEV, Y. D. 2012*b* The dynamics of liquid drops and their interaction with solids of varying wettabilities. *Phys. Fluids* **24**, 082001.

SPRITTLES, J. E. & SHIKHMURZAEV, Y. D. 2012*c* A finite element framework for describing dynamic wetting phenomena. *Intl J. Numer. Meth. Fluids* **68**, 1257–1298.

SPRITTLES, J. E. & SHIKHMURZAEV, Y. D. 2013 Finite element simulation of dynamic wetting flows as an interface formation process. *J. Comput. Phys.* **233**, 34–65.

SPRITTLES, J. E. & SHIKHMURZAEV, Y. D. 2014*a* Dynamics of liquid drops coalescing in the inertial regime. *Phys. Rev.* E **89**, 063006.

SPRITTLES, J. E. & SHIKHMURZAEV, Y. D. 2014*b* A parametric study of the coalescence of liquid drops in a viscous gas. *J. Fluid Mech.* **753**, 279–306.

SUNDARARAJAKUMAR, R. R. & KOCH, D. L. 1996 Non-continuum lubrication flows between particles colliding in a gas. *J. Fluid Mech.* **313**, 283–308.

TANNER, L. H. 1979 The spreading of silicone drops on horizontal surfaces. *J. Phys. D: Appl. Phys.* **12**, 1473–1484.

THORODDSEN, S. T., ETOH, T. G. & TAKEHARA, K. 2005 The air bubble entrapped under a drop impacting on a solid surface. *J. Fluid Mech.* **545**, 203–212.

VANDRE, E., CARVALHO, M. S. & KUMAR, S. 2012 Delaying the onset of dynamic wetting failure through meniscus confinement. *J. Fluid Mech.* **707**, 496–520.

VANDRE, E., CARVALHO, M. S. & KUMAR, S. 2013 On the mechanism of wetting failure during fluid displacement along a moving substrate. *Phys. Fluids* **25**, 102103.

VANDRE, E., CARVALHO, M. S. & KUMAR, S. 2014 Characteristics of air entrainment during dynamic wetting failure along a planar substrate. *J. Fluid Mech.* **747**, 119–140.

VELARDE, M. G. 2011 Discussion and debate: wetting and spreading science – quo vadis? In *The European Physical Journal Special Topics* (ed. M. G. Velarde), vol. 197. Springer.

VOINOV, O. V. 1976 Hydrodynamics of wetting. *Fluid Dyn.* **11**, 714–721.

WEINSTEIN, S. J. & RUSCHAK, K. J. 2004 Coating flows. *Annu. Rev. Fluid Mech.* **36**, 29–53.

WILSON, M. C. T., SUMMERS, J. L., SHIKHMURZAEV, Y. D., CLARKE, A. & BLAKE, T. D. 2006 Nonlocal hydrodynamic influence on the dynamic contact angle: slip models versus experiment. *Phys. Rev.* E **83**, 041606.

XU, L. 2007 Liquid drop splashing on smooth, rough, and textured surfaces. *Phys. Rev.* E **75**, 056316.

XU, L., ZHANG, W. & NAGEL, S. R. 2005 Drop splashing on a dry smooth surface. *Phys. Rev. Lett.* **94**, 184505.

YARIN, A. L. 2006 Drop impact dynamics: splashing, spreading, receding, bouncing. *Annu. Rev. Fluid Mech.* **38**, 159–192.

https://doi.org/10.1017/jfm.2015.121 Published online by Cambridge University Press